Interactive discussion on AMTD-2017-286 "Spatial distribution analysis of the OMI aerosol layer height: a pixel-by-pixel comparison to CALIOP observations"

Julien Chimot *et al.*

J.J.Chimot@tudelft.nl

We thank Referee #1 for his / her valuable comments. They give us the opportunity to solidify our messages and manuscript. Below we address them one by one (Referee #1 comments in blue, author and co-authors in black).

The paper discusses the application and evaluation of a novel technique to retrieve a measure of aerosol layer height based on a Neural Network based technique. Overall, the paper is well written and should be published after the authors address my, mostly-minor, comments below.
My main comment has to do with the evaluation of retrieved dust layer height and the uncertainty analysis.

We took into account all the comments and questions asked by Referee #1 below. We reformulated where necessary according to the remarks and question, in order to ensure a better clarification. More details on these reformulations are given below where appropriate.

I do not understand why they have chosen events during periods (post row-anomaly) when the evaluation using CALIOP data is impossible. The authors should re-do their analysis of the OMI NN dust- retrieval method making use of observations between the launch of CALIOP (mid-2006) and the beginning of the OMI row anomaly problem by the end of 2008.

Following the referee suggestion, we selected another Saharan dust case study occurring prior to the OMI row anomaly development. This time, we mostly focused on diverse cases occurring in July 2007 and selected the day 2007.07.19, one of the days with a low cloud coverage and the large size of dust plume over the Atlantic ocean. Overall, the conclusions remain unchanged apart of the maximum distance between OMI pixels and the CALIOP track which is reduced from 300 km to 100 km.
The average difference (OMI-CALIOP) ALH is -350 m. However, this difference shows quite some large variabilities with a standard deviation of 2.1 km and a low correlation (smaller than 0.4).
We would like to stress that dust particles which are coarse (more than absorbing particles released by fires or nitrate and sulfate resulting from urban and industrialized pollution episodes) and irregularly shaped (thus non-spherical as assumed by the Henyey-Greenstein phase function) are not included in the dataset used for training the NN algorithms. This can lead to significant biases with respect to the modelled scattering phase function. In addition, the use of a prior AOD from MODIS sensor based on a different aerosol model, potentially also inaccurate for pure dust, may lead to some inconsistencies. The resulting impacts may be larger on this case than on wildfires or urban pollution events where released particles generally have a more spherical shape. We propose then to replace the Fig. 9 of our discussion manuscript by the Fig.9 below in our final manuscript.

Please read more below regarding our answer to question of the referee about this specific topic.

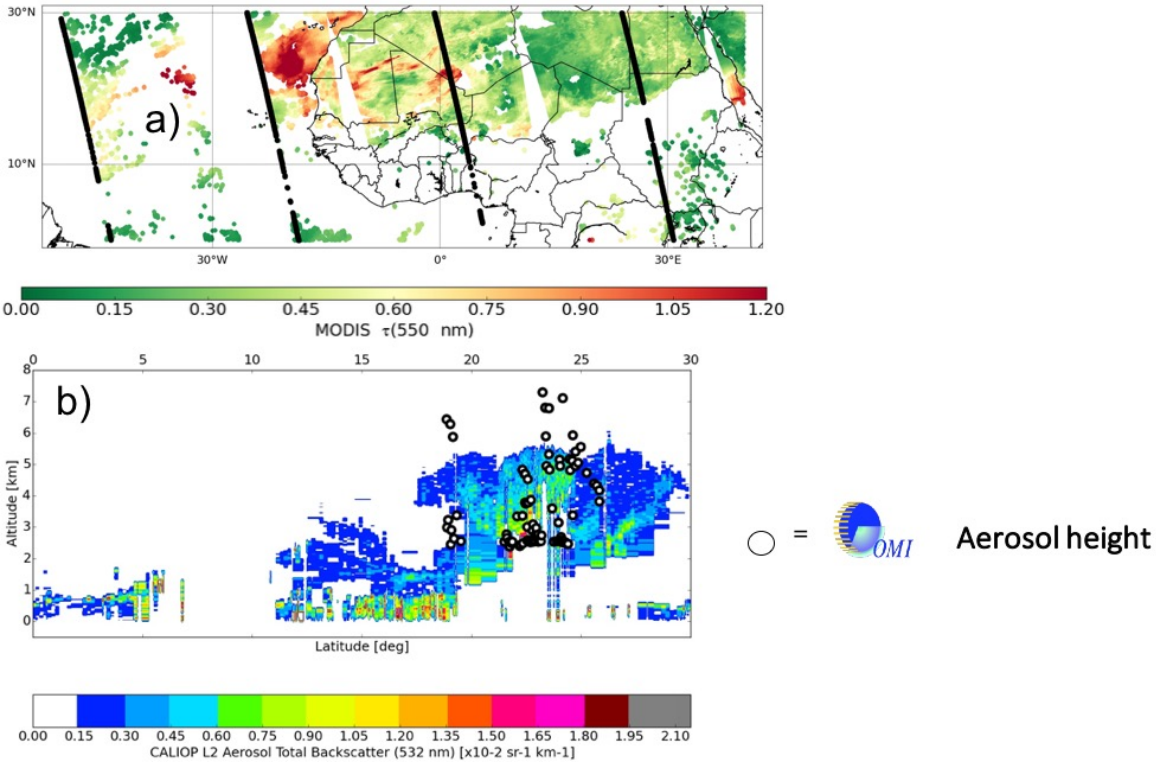

Figure 9: Elevated layer due to a Saharan dust outbreak transported to Western Mediterranean region over sea on 2007.07.19: (a) Map of MODIS Aqua τ (550nm) from the combined DT DB Collection 6 (cf. Sect. 2.3), (b) Retrieved OMI ALH compared with vertical profile of aerosol total backscatter coefficient (532 nm) from the CALIOP L2 aerosol total backscatter (532 nm) associated with the 1st left CALIPSO track over sea in Fig. 9a.

The authors have discussed an uncertainty analysis associated with the assumed values of physical parameters used in the generation of NN training data sets. No error analysis, however, is performed regarding AOD. There seems to be an implicit assumption that the MODIS provided AOD is error-free. There are two ways the uncertainty of the MODIS AOD will propagate to the OMI ALH retrieval:
1) Uncertainty of the MODIS algorithm associated with assumptions on surface albedo, SSA and particle size and shape. Over the oceans, MODIS uncertainties in surface albedo and angstrom exponent are generally very low. The effect of particle shape, however, is non-negligible. Assumed SSA albedo is another source of error. MODIS retrievals over land are subject to uncertainties to all above listed parameters.

As discussed in our manuscript (*cf.* Sect 2.2), an accurate AOD information is required to retrieved ALH from OMI as both AOD and ALH simultaneously drive the O_2-O_2 slant column density (SCD) N_5O_2-O_2. Therefore, retrieving ALH without information on AOD would lead to an ambiguity. The way how an uncertainty on prior AOD impacts the OMI ALH retrieval was already extensively analyzed in Chimot *et al.* (2017). We judged that it was not relevant to repeat this sensitivity analysis in the present manuscript. However, from this study, we mentioned at the end of Sect. 2.2 an accuracy of 0.2 is necessary on the prior τ(550 nm) parameter. We have well in mind that MODIS AOD is not error free.

2) Even if all internal MODIS algorithm uncertainties are well characterized and propagated to the NN ALH retrieval, there is still the issue of the spectral consistency of the assumed aerosol models. Is the NN algorithm designed to assume the same aerosol type as identified by the MODIS algorithm? There may be cases, particularly over land, when the algorithms select different aerosol types. The use of MODIS- AOD for a particular model may not be reasonable for the OMI NN assumed model. It would therefore be desirable to have a consistent retrieval algorithm providing both the AOD and ALH.
Please elaborate on the above-stated points.

We fully agree here with the remark of the referee. The mismatch between the model used for the prior AOD estimation and the one employed for the ALH retrieval may lead to some inconsistencies. However, such an issue is highly challenging and very difficult to properly characterize and estimate.

Our aerosol NN algorithms were designed by using aerosol models regardless of the information sources of all the input variables, *e.g.* AOD or surface albedo. Our main aim was to explore the potential of combining the OMI visible O_2-O_2 absorption band and a machine learning approach to retrieve an ALH parameter. Theoretically, one can run these algorithms with an AOD product derived from any sensor or model. However, our previous study showed how crucial is this AOD quality to mitigate the ALH retrieval bias.
We acknowledge that any mismatch between the MODIS AOD aerosol and the OMI ALH aerosol models can lead to some inconsistencies, and, at the end, not only to some uncertainties but also potential strange patterns in our retrieval. This could even be worse if both models are very far from the true aerosol mixture properties present in the scene and/or differ very much regarding the modelling of the scattering phase function. In addition, one should not exclude other auxiliary datasets that are used for both MODIS AOD and OMI ALH retrievals and could increase these consistencies: *e.g.* surface albedo or directional reflectance.

One cannot exclude that an inconsistency problem may actually occur in the analyzed Saharan dust case. However, since pure dust particles are not included in the training dataset of these NN algorithms, it is difficult to identify such a feature. Nevertheless, we do not see such problems in our other cases and related analyses. Therefore, we think that potential inconsistencies are, at this stage, not critical. But we agree that future developments or improvements or our NN OMI aerosol algorithms should take into consideration the consistency between the aerosol model in the training dataset and the assumed prior parameters.

Other comments:
Page 3, line 4 suppress 'ideally'
Done

Page 3, line 18 add 'channel' after O_2-O_2
Added

Page 3, line 19 replace 'the present' with 'the current'
Done

Page 3, line 20-21, last sentence is paragraph is confusing and actually unnecessary. Remove it.
Done

Page 5, line 24, provide a reference (or elaborate on performed sensitivity analyses by the authors) to substantiate the statement that the AMF does not depend on the aerosol scattering phase function.
We do not have specific references that directly show the low sensitivity of the tropospheric NO2 AMF to the scattering phase function. However, we do have several references (Leitao *et al.*, 2011; Castellanos *et al.*, 2015; Chimot *et al.*, 2016) that showed the low sensitivity to aerosol single scattering albedo, Angstrom coefficient, and asymmetry parameter. All these studies and our experience in radiative transfer modelling with the involved KNMI experts do suggest then this statement.
We added these references on Page 5, Line 24.

Page 8, line 12, spectral characterization applies to the radiation not to the particles. Please rephrase.
The word "absorbing" was missing in the former statement. We reformulated as follows:
"Therefore, we use the NN algorithm trained with ω0 = 0.95 assuming low abundance of UV and visible absorbing particles."

Page 8, line 26, use the 1064 nm measurement instead of the 532 one. It has been shown by several publications that the CALIOP's 532 attenuated backscatter signal attenuates very rapidly in the presence of smoke layers and, therefore, does not capture the full vertical extent of the layer.
Page 9, lines 28-30 and Page 10, lines 1 to 8. This is not a new finding. Problems with the CALIOP 532 nm measurement have been demonstrated by the quoted literature. The authors should just work with the 1064 channel that works well for all aerosol types.

Indeed, we found publications mentioning the specific problem of CALIOP'532 nm signal and we cite them in our manuscript accordingly. However, our experience on these cases with the OMI ALH retrieval and its comparison with CALIOP L2 and L1 seems to teach us that this problem is mostly known by the research community working with active satellite sensor, and somehow less by the scientists involved with passive sensors, or at least by the persons in trace gas studies.
Furthermore, we would like to draw the attention of the referee to the importance of distinguishing the CALIOP 1064 attenuated backscatter signal (i.e. level 1 – L1 - product) and aerosol backscatter signal (i.e. level 2 – L2). Although the CALIOP 1064 L1 signal probes the full vertical extent of the smoke layer (see our Figs. 7d and 8), the CALIOP 1064 L2 product is actually hampered and limited to the top layer similarly to the CALIOP 532 channel (see Fig. 7b). This is due to the fact that aerosol retrieval in both channels requires first the aerosol characterization which is based on the 532 nm channel (cf. Sect. 2.3). Since it is attenuated in the lower layers, the aerosol extinction retrieval from the CALIOP 1064 nm channel is not applied in these specific layers. Therefore, the CALIOP 1064 nm L2 does not contain the full aerosol vertical profile and cannot either be used for our comparison study. This specific problem was also confirmed *via* a personal communication with Dr. Marc Vaughan who has been strongly involved in the Level 2 CALIOP algorithms.

We already mentioned this point, at a high level, in Sect 3.3., 2nd paragraph.

Page 10, lines 19-27. The poor performance of CALIOP's 532 nm channel is mostly instrumental (i.e., low laser power). As shown by Kacenelenbogen et al. [2011], the HSRL 532 nm channel works equally well for all aerosol types.
Yes, we agree that the 1st (and likely main) problem comes from the low CALIOP Signal-to-Noise Ratio (SNR) and thus prevents to probe tenuous absorbing aerosol plumes. The resulting signal may be likely driven below CALIOP's detection threshold indicating then an instrumental feature. However, we are not completely sure that only this element explains the difference between OMI (a passive sensor with some noise as well) and the CALIOP active instrument. The question of using then a more powerful laser source to circumvent this problem may remain then open. Hopefully, we will have an answer with the future LIDAR space-borne sensors (*e.g.* EarthCare).
Also, we would like to invite the reader to keep in mind that the physical information from a passive spectral measurement contains some differences: *e.g.* the importance of multiple *vs.* single scattering effects included in both measurements.

Page 10, line 28. CALIOP data should not be used to evaluate the NN OMI ALH product because of the loss of OMI-CALIOP collocation after Dec 2008 due to the onset of the row anomaly. There are however, 30 months of data (July 2006 to Dec 2008) that offer hundreds of dust events when full OMI-CALIOP collocation is possible. The authors should replace the currently used post-2008 case studies, with pre-2009 events. Dust activity is seasonal. Therefore, it is not difficult to find 'good' dust cases in the pre-row anomaly period of OMI observations.
This is acknowledged. Please see our discussions earlier in this document.

Interactive discussion on AMTD-2017-286 "Spatial distribution analysis of the OMI aerosol layer height: a pixel-by-pixel comparison to CALIOP observations"

Julien Chimot *et al.*

J.J.Chimot@tudelft.nl

We thank Referee #2 for his / her comments. Below we address them one by one (Referee #2 comments in blue, author and co-authors in black).

The paper presents the retrievals of aerosol layer height from OMI O_2-O_2 absorbing band and evaluate the retrievals with CALIOP. The retrieval method was published already, which is based on neutral network algorithm trained with data from radiative transfer calculation. Overall, the paper is interesting, and I recommend it be published after the following comments are addressed.

We took into account all the comments and questions asked by Referee #2 below. We reformulated where necessary according to the remarks and question, in order to ensure a better clarification. More details on these reformulations are given below where appropriate.

1) The introduction part discussed pros and cons O_2 A band. how about O_2 B? Both Xu *et al.* (2017, cited already) and Ding *et al.* (2016, see below) showed from real data and theoretical calculation that O_2 A and B are complimentary to each other for retrieving ALH at different altitude. This is because their combination provides a wider range of different O_2 optical depth, thereby allowing to characterize aerosol layer at different altitude. I recommend that both Xu's paper and Ding's paper should be added in the introduction to talk about O_2 B band.

Ding, S. *et al.*, 2016, Polarimetric remote sensing in O_2 A and B bands: Sensitivity study and information content analysis for vertical profile of aerosols, Atmospheric Measurement Techniques, 9, 2077-2092, doi:10.5194/amt-9-2077-2016.

Thank for the reference. We, the authors, have much less experiences with the O_2-B spectral band than the O2-A for now. However, the paper of Ding *et al.* (2016) suggests, like Xu *et al.* (2017), that there is indeed a possibility to exploit it in synergy with the O_2-A. Its proximity with the O_2-A may suggest similar difficulties (high surface albedo over land, low AOT compared to the O_2-O_2). Moreover, Ding et al. (2016) suggest a lower optical depth and thus signal. However, we are very much in favor and encourage all studies investigating the amount of information on aerosol height that can be derived, and the corresponding approaches necessary for that purpose.
We added a sentence mentioning this reference and this band in the introduction, on Page 3.

2) Equation 1. Comparing ALH with CALIPO. Xu *et al.* (2017) used the same method to evaluate ALH retrieved EPIC/DSCOVR, and their better found a better statistics, although their analysis over the over ocean. In case of O_2-O_2 method, this reviewer is curious how well the final results (using AHL and AOD for forward calculating) can agree with OMI spectra in O_2-O_2? Because O_2-O_2 absorption optical depth is small, it has the disadvantages to retrieve high altitude aerosol layer. Is there any limit where retrieval uncertainty is too large? Regardless, some discussion on how the results compare with some existing techniques can be more helpful to the readers.
As investigated in Chimot *et al.* (2017) and mentioned in this manuscript in Sect2.2., reliable OMI ALH is available over scenes with a minimum AOT(550 nm) value of 0.5. Below this threshold, the aerosol load has too little effects on the absorption by the dimers at 477 nm. Moreover, since the O_2 collision complex absorption scales with the pressure-square instead of being linear with pressure, there is very little sensitivity for aerosol layers located at high altitude: *i.e.* approximately above 5 km (Park *et al.*, 2016). Also, cloudy scenes and too bright surfaces such as deserts and snow should be discarded.

A direct comparison with other techniques would deserve a rigorous study in itself. At high level, we can say that the 477 nm O2-O2 spectral band present the advantages of higher AOT values, and lower surface albedo over land surfaces. The lack of contrast between surface reflectance and scattering

layers in the Near-InfraRed (NIR) usually leads to several challenges over non dark surfaces such as vegetation. We briefly discussed these advantages in the Introduction, Page 3 Lines 16-20.

3) How the shape of aerosol profile is defined? Is it Gaussian distribution, and how the width of profile is assumed? In Xu et al. (2017), the assumption of the width is based on field data. Globally, will the width have any effect on retrieval?

The aerosol profile shape is described in Chimot *et al.* (2017) and already repeated in the present manuscript in Sect.2.2 Line 31: "Aerosol profiles are assumed as one single scattering layer (also called "box-layer") with a constant geometric thickness (100 hPa, or about 1 km). The particles included in this layer are homogeneous (*i.e.* same size and optical properties). ALH is then defined as the mid-altitude (above sea level) of this scattering layer.". A different profile shape such as Gaussian or 2 separate layers as investigated in Sect.4.2. and Fig.s.11-12 could indeed impact somehow the ALH retrieval. Overall, we show in this manuscript that ALH is a weighted average of the aerosol extinction coefficients, in the visible, distributed along the vertical atmospheric layers. Overall, all our analyses demonstrate that aerosol model, and then potential cloud residuals, are the most crucial assumptions affecting the quality of the OMI ALH derivation.

4) In several plots, the retrieved AHL appears to be for aerosols above clouds (such as Figure 7 -14 - -12 degree). In such cases, how AHL from CALIOP is computed? Cloud contamination seems very high in all cases showed.

The ALH of CALIOP is exclusively computed from the CALIOP L2 aerosol product, which does not contain the layers identified as clouds by the CALIOP processing chain. Therefore, the CALIOP ALH is only based on aerosol layers. In all the cases we have selected and analyzed, we tried as much as possible to detect and filter-out collocated OMI-MODIS cloud scenes following the methodology described in Sect.2.3. Of course, we acknowledge that, in spite of these efforts, some cloud residuals may persist, and this is why we studied the potential impacts in Sect.4.5 and Fig.14.

However, given the reasonable agreement we obtained between OMI and CALIOP ALH and our analyses, the number of selected OMI pixels with aerosols above clouds is expected to be quite minimal in this manuscript.

5) Non-spherical dust phase function. It is surely important, but in many cases, especially in Asia, dust and spherical particles can co-exist, and only consider non-spherical particles are not sufficient as shown in the following paper. Does the difference bewteen AHL vs. CALIOP counterparts as a function of scatting albedo show any indication of dust non-spherical effect? It will be interesting to see if the difference as scattering angle is flat or random for smoke particles.

As discussed in our manuscript and our precedent study, the aerosol model accuracy plays a crucial role in the quality of the OMI ALH retrieval. This covers the optical properties such as scattering *vs.* absorption (*cf.* single scattering albedo), but also the realism of the scattering phase function.

Dust can be often mixed with nitrate and sulfate, especially over large industrialized and urban area such in East-Asia, and in Spring and Summer during the dust transport episodes from the deserts. However, anthropogenic particles still dominate the measured signals in these regions. As stipulated in our outlook, we advised indeed in future studies to consider more aerosol models and detailed scattering phase function modelling (*e.g.* Mie scattering for spherical particles and T-Matrix for pure dust outbreak). New neural networks should be then trained based on these new datasets and their performances on smoke cases could be then compared in detail with the present performances.

Wang, J. *et al.*, 2003, The effects of non-sphericity on geostationary satellite retrievals of dust aerosols, Geophys. Res. Lett., 30, 2293.

We thank the Referee for informing us about this last reference.

Spatial distribution analysis of the OMI aerosol layer height: a pixel-by-pixel comparison to CALIOP observations

Julien Chimot[1,*], J. Pepijn Veefkind[1,2], Tim Vlemmix[2], and Pieternel F. Levelt[1,2]

[1]Department of Geoscience and Remote Sensing (GRS), Civil Engineering and Geosciences, TU Delft, the Netherlands
[2]Royal Netherlands Meteorological Institute, De Bilt, the Netherlands
[*]now at European Organisation for the Exploitation of Meteorological Satellites (EUMETSAT), Darmstadt, Germany

Correspondence to: Julien Chimot (Julien.Chimot@eumetsat.int)

Abstract. A global picture of atmospheric aerosol vertical distribution with a high temporal resolution is of key importance not only for climate, cloud formation and air quality research studies, but also for correcting ~~aerosol radiation effect~~ scattered radiation induced by aerosols in absorbing trace gas retrievals from passive satellite sensors. Aerosol layer height (ALH) was retrieved from the OMI 477 nm $O_2{-}O_2$ band and its spatial pattern evaluated over selected cloud-free scenes. Such retrievals benefit from a synergy with MODIS data to provide complementary information on aerosols and cloudy pixels. We used a neural network approach previously trained and developed. Comparison with CALIOP aerosol level 2 products over urban and industrial pollution in east China shows consistent spatial patterns with an uncertainty in the range of 462-648 m. In addition, we show the possibility to determine the height of thick aerosol layers released by intensive biomass burning events in South-America and Russia ~~, and of a~~ from OMI visible measurements. A Saharan dust outbreak over sea ~~from OMI visible measurements~~is finally discussed. Complementary detailed analyses show that the assumed aerosol properties in the ~~modeling~~ forward modelling are the key factors affecting the accuracy of the results, together with potential cloud residuals in the observation pixels. Furthermore, we demonstrate that the physical meaning of the retrieved ALH scalar corresponds to the weighted average of the vertical aerosol extinction profile. These encouraging findings strongly suggest the potential of the OMI ALH product, and in more general the use of the 477 nm $O_2{-}O_2$ band from present and future similar satellite sensors, for climate studies as well as for future aerosol correction in air quality trace gas retrievals.

1 Introduction

Aerosols are small particles suspended in the air (e.g. desert dust, sea salt, volcanic ashes, sulfate, nitrate and smoke from biomass and fossil fuel burning). Aerosol sources and sinks are heterogeneously distributed. Due to their scattering and absorption effects on solar and thermal radiation, they redistribute shortwave radiation in the atmosphere. Their presence not only perturbs the air thermal state and stability, our climate system, air quality and meteorological conditions, but also interferes with satellite observations of atmospheric trace gases. Aerosols are an important player in the climate system by leading to atmospheric warming, surface cooling and additional atmospheric dynamical responses (IPCC: The Core Writing Team Pachauri and Meyer, 2014). By acting as the condensation nuclei on which clouds form, they also modify cloud formation, lifetime and precipitation (Figueras i Ventura and Russchenberg, 2009; Sarna and Russchenberg, 2017). Overall, the climate effects of

aerosols are large, but the scientific understanding of their effects remains challenging as their radiative properties is one of the main uncertain components in global climate models (Yu et al., 2006; IPCC: The Core Writing Team Pachauri and Meyer, 2014). Finally, the scattering and absorption by aerosols impact the actinic flux, and consequently modifies the photolysis rates of important processes in the atmosphere (Palancar et al., 2013).

In addition, scattering and absorption of shortwave radiation by aerosols modify the average light path in the atmosphere, and therefore interfere with satellite observations of gases, such as NO_2, SO_2, O_3, CO_2, and CH_4, which are important for air quality and climate science objectives. Europe is heavily investing in the development of polar orbiting and geostationary satellite systems in the Copernicus program (Ingmann et al., 2012), which will form an important component of air-quality and climate observing system from urban, regional to global scale (Martin, 2008; Duncan et al., 2014). However, inaccurate aerosol correction on these satellite measurements leads to misinterpretations and incorrect evaluations of the implemented emission regulation controls.

The magnitude of the radiative forcing by aerosols depends on the environmental conditions, aerosol properties and horizontal and vertical distribution (IPCC: The Core Writing Team Pachauri and Meyer, 2014; Kipling et al., 2016). Its determination requires satellite data in addition to models (IPCC: The Core Writing Team Pachauri and Meyer, 2014). While, overall, the horizontal distributions of aerosol optical depth (AOD or τ) and size are relatively well constrained, uncertainties in vertical profile significantly contribute to the overall uncertainty of radiative effects, e.g. 25 % of the uncertainty of black carbon radiative estimations from the models is related to an inaccurate knowledge on the vertical distribution (McComiskey et al., 2008; Loeb and Su, 2010; Zarzycki and Bond, 2010; IPCC: The Core Writing Team Pachauri and Meyer, 2014). Knowledge of aerosol vertical profiles allows the computation of related heating rates: e.g. particles located above clouds can increase the liquid water path and geometric thickness of clouds and the subsequent atmospheric heating; advection of light-absorbing aerosols over the ocean and clouds from rice straw burning in China can strongly reduce clouds and Earth radiant energy (Hsu et al., 2003; de Graaf et al., 2012; Wilcox, 2012). Therefore, aerosol layer height (ALH) drives not only the magnitude but also the sign of aerosol direct and indirect radiative effects (Kipling et al., 2016). Current ALH simulated by climate models can differ in the range of 1.5-3 km (Koffi et al., 2012; Kipling et al., 2016).

Furthermore, in the absence of clouds, vertical distribution of aerosols is one of the most significant error sources in trace gas retrievals from satellites (Leitão et al., 2010; Chimot et al., 2016). Major biases on the pollutant tropospheric NO_2 measured by satellites, depending on AOD and ALH, can be expected if no aerosol correction is applied. Because such information is not available for every observation, aerosols are approximated via a simple cloud model (Acarreta et al., 2004; Boersma et al., 2011; Veefkind et al., 2016). This only leads to a first-order correction for short-lived gases (NO_2, SO_2, and $HCHO$), that does not comprehensively assume the full scattering and absorbing effects of aerosol particles on the average light path followed by the detected photons (Boersma et al., 2011; Chimot et al., 2016). Especially, current uncertainties on ALH leads to substantial biases in areas with high AOD (~~$>$~~ $\tau(550\ nm) \geq 0.5$), and absorbing and elevated particles: between -26 % and -40 % on the retrieved tropospheric NO_2 columns from the Dutch Finnish Ozone Monitoring instrument (OMI) (Castellanos et al., 2015; Chimot et al., 2016), 20-50 % on Global Ozone Monitoring Experiment-2 (GOME-2) and SCIAMACHY $HCHO$ (Barkley et al., 2012; Hewson et al., 2015), about 50 % on OMI SO_2 (Krotkov et al., 2008). ALH also remains one of the largest error

sources for greenhouse gas retrievals: e.g. CO_2 from the American carbon OCO-2 mission (Crisp, 2015; Connor et al., 2016; Wunch et al., 2017) and CH_4 from the future TROPOMI on-board Sentinel-5 precursor (Hu et al., 2016).

Consequently, determining ALH with a large coverage (ideally daily and global) and an uncertainty better than 1 km (as a first approximation), for every single absorbing trace gas atmospheric satellite pixel, is ideally needed. Active satellite sensors, such as the Cloud-Aerosol Lidar with orthogonal Polarization (CALIOP), allow to probe detailed vertical aerosol profile, but with a limited coverage as they only look towards the nadir. This can lead to a gap up to 2200 km (in the tropics and subtropics) between adjacent orbital tracks. As an alternative, passive satellite sensors, with a high spectral resolution such as OMI, offer adequate spatial coverage with a good temporal resolution (up to daily-global before the OMI row anomaly development) thanks to a wide swath. Thus, passive hyperspectral instruments can provide great contribution even if they do not achieve the same level of accuracy as active instruments (i.e. limited vertical resolution, only cloud-free scenes). Because molecular oxygen (O_2) is well mixed, its slant column measurement provides with a suitable proxy for the determination of the modified scattering height due to aerosols, in absence of clouds. Most of the developed ALH retrieval algorithms from backscattered sunlight satellite measurements focus on the absorption spectroscopy of the O_2-A band around 765 nm, relatively close to the CO_2 and CH_4 absorption bands (Wang et al., 2012; Sanders et al., 2015). Some studies also focus on the use of the O_2-B band (Ding et al., 2016; Xu et al., 2017). So far, only a few studies have yet worked on using the $O_2{-}O_2$ satellite absorption bands, within the ultraviolet (UV) and visible (vis) spectral ranges, to retrieve ALH and τ (Park et al., 2016; Chimot et al., 2017). These bands are spectrally closer to the NO_2, SO_2 and HCHO absorption lines. Contrary to the O_2-A band, the $O_2{-}O_2$ 477 nm band presents a wider (over 10 nm) although weaker spectral absorption. This leads to high sensitivities in case of strong aerosol loading and with less challenges due to saturation. Moreover, in the visible spectral range, AOD values are generally higher while surface albedo or reflectance is lower leading then to a higher contrast between aerosol and surface scattering signals. The 477 nm $O_2{-}O_2$ channel is not only present in the ~~present~~ current GOME-2, OMI and TROPOMI satellite sensors, but will be also included in the future Sentinel-4 and Sentinel-5 instruments (Ingmann et al., 2012; Veefkind et al., 2012). ~~They should be then more studied in detail in terms of information content about particles.~~

This paper follows the exploratory study of Chimot et al. (2017) where a neural network (NN) algorithm ~~has been~~ was developed to investigate the feasibility of deriving ALH from the OMI 477 nm $O_2{-}O_2$ spectral band over cloud-free scenes. The main objective was the study of anthropogenic particles emission and their precursors from vehicles, coal burning, and industries. It has allowed to retrieve ALH over land for the first time from this specific spectral band. A statistic evaluation of 3-year cloud-free OMI observations over east Asia, focusing on urban and large industrialized areas, has shown maximum differences below 800 m with a reference climatology database. In order to complete this first and statistically-focused evaluation, the present study evaluates the spatial distribution of the OMI 477 nm $O_2{-}O_2$ ALH product on a pixel-by-pixel basis. It therefore focuses on its variability for single days. For that purpose, specific cloud-free case studies are selected including three winter days with strong anthropogenic pollution over east China. In addition, to extend the performance assessment of such an approach beyond the initial objective of Chimot et al. (2017), new types of aerosol pollution episodes are investigated: four summer days with large biomass burning events in South-America and east of Russia, and one day of wide desert dust

transport over sea. The OMI ALH retrieval is compared with the collocated CALIOP level 1 (L1) measurements and level 2 (L2) aerosol retrievals.

2 OMI, MODIS and CALIOP aerosol observations

2.1 The OMI sensor and O_2-O_2 477 nm spectral band

The Dutch-Finnish OMI mission (Levelt et al., 2006) is a nadir-viewing push-broom imaging spectrometer launched on the National Aeronautics and Space Administration (NASA) Earth Observing System (EOS)-Aura satellite. It delivers global coverage with a high temporal resolution of key air quality components derived from measurements of the backscattered solar radiation acquired in the UV-Vis spectral domain (270-550 nm) with approximately 0.5 nm resolution. Based on a two-dimensional detector array concept, radiance spectra are simultaneously measured on a 2600 km wide swath within a nadir pixel size of 13x24 km^2 (28x150 km^2 at extreme off-nadir).

The O_2-O_2 477 nm absorption band is currently operationally exploited by the OMI O_2-O_2 cloud algorithm (OMCLDO2) to derive effective cloud parameters (Acarreta et al., 2004; Veefkind et al., 2016). This spectral band directly measures the absorption of the visible part of the sunlight induced by the O_2-O_2 collision complex along the whole light path. A spectral fit, prior to the OMI effective cloud retrieval algorithm, is performed over the 460-490 nm spectral range to derive the continuum reflectance $R_c(475\,\mathrm{nm})$ and the O_2-O_2 slant column density $N^s_{O_2-O_2}$. This spectral fit relies on the differential optical spectroscopy (DOAS) approach (Platt and Stutz, 2008). $N^s_{O_2-O_2}$ represents the O_2-O_2 absorption magnitude along the average light path through the atmosphere. This is the key input variable for the OMI ALH retrieval by the NN algorithm.

2.2 The OMI aerosol layer height neural network algorithm

The OMI ALH retrieval algorithm (Chimot et al., 2017) is based on the exploitation of $N^s_{O_2-O_2}$ derived from the DOAS fit, and relies on a NN approach. Here, the main elements of this algorithm are summarized but for more details about their technical development and implementation, the reader is encouraged to read (Chimot et al., 2017).

~~These algorithms rely~~ This algorithm relies on how aerosols affect the length of the average light path along which the O_2-O_2 absorbs. $N^s_{O_2-O_2}$ is then driven by the overall shielding or enhancement effect of photons by the O_2-O_2 complex in the visible spectral range, due to the presence of particles. An aerosol layer located at high altitudes ~~will apply~~ applies a large shielding effect on the O_2-O_2 located in the atmospheric layers below: i.e. the amount of photons coming from the top-of-atmosphere and reaching the lowest part of the atmosphere is reduced compared to an aerosol-free scene. This shielding effect is then larger when the aerosol layer is located at an elevated altitude than close to the surface.

The designed NNs belong to the family of machine learning and the artificial intelligence domain and rely on a multi-layer architecture, also named multilayer perceptron. The input and output variables are inter-connected through a set of sigmoid functions present in the hidden layers and the synaptic weights W. For each single sigmoid function, two simple operations

are performed: 1) a weighted sum of all the inputs given by the previous layer, 2) a transport of this sum through the sigmoid functions. The ALH retrieval problem then becomes a simple series of analytical functions.

~~Aerosol profiles are~~ For all the processed OMI scenes, aerosol profile is assumed as one single scattering layer (also called "box-layer") with a constant geometric thickness (100 hPa, or about 1 km). The particles included in this layer are homogeneous (i.e. same size and optical properties). ALH is then defined as the mid-altitude (above sea level) of this scattering layer. Furthermore, aerosol particles are assumed to cover the entire satellite observation pixel. The input layer contains 7 parameters: viewing zenith angle θ, solar zenith angle θ_0, relative azimuth angle ϕ_r, surface pressure Ps, surface albedo A, aerosol optical thickness $\tau(550\mathrm{nm})$ and the OMI $N^{\mathrm{s}}_{\mathrm{O_2-O_2}}$. As explained in Chimot et al. (2017), a prior $\tau(550\mathrm{nm})$ is required as input as both ALH and $\tau(550\mathrm{nm})$ simultaneously affect $N^{\mathrm{s}}_{\mathrm{O_2-O_2}}$ and need to be distinguished.

The optimal weights were estimated through a rigorous training task following the error-back propagation technique and a training data set that includes a set of representative situations for which inputs and outputs are well known. The quality of the training data set was ensured by full-physical spectral simulations, dominated by aerosol particles without clouds, generated by the Determining Instrument Specifications and Analyzing Methods for Atmospheric Retrieval (DISAMAR) software of KNMI (de Haan, 2011). Aerosol scattering is simulated by a Henyey–Greenstein (HG) scattering phase function $\Phi(\Theta)$ parameterized by the asymmetry parameter g, which is the average of the cosine of the scattering angle (Hovenier and Hage, 1989). Aerosols were specified for a standard case, assuming fine particles with a unique value of the extinction Ångström exponent $\alpha = 1.5$ and $g = 0.7$. In order to investigate the assumptions related to the aerosol single scattering albedo ω_0 properties, two training data sets were generated with a different typical value: one with $\omega_0 = 0.95$ and one with $\omega_0 = 0.9$ in the visible spectral domain. Therefore, two OMI ALH NN algorithms ~~have been~~ were created, one for each aerosol ω_0 values.

The aerosol models in the training database were based on a Henyey-Greenstein scattering phase function for two reasons: 1) both Chimot et al. (2017) and this manuscript are exploratory studies focusing on the potential of exploiting the $\mathrm{O_2-O_2}$ spectral band for aerosol retrievals from a satellite sensor, 2) our first long-term objective is the potential use of the ALH parameter for future tropospheric $\mathrm{NO_2}$ and similar trace gas retrievals over cloud-free scenes. Several studies emphasized that ALH is the key variable affecting the length of the average light path in the computation of the related air mass factor (AMF) computation through the DOAS approach (Boersma et al., 2004; Castellanos et al., 2015; Chimot et al., 2016). This is because the only quantity that is relevant for absorption by trace gases in the visible is the average light path distribution, i.e. the distribution of distances traveled by photons in the atmosphere before leaving the atmosphere. The absolute radiance at the top of the atmosphere (TOA) is less important. The second variable of interest is τ. This average light path distribution is mostly governed by ω_0 and g, and of course ALH and τ, much less by details in the phase function. ~~Those two scattering parameters~~ Studies by Leitão et al. (2010); Castellanos et al. (2015); Chimot et al. (2016) showed the lower sensitivity of the AMF to α, ω_0 and g. These scattering parameters are included in HG scattering, and therefore ~~it~~ this parametrized phase function can be used for AMF calculations. At this level and with respect to these mentioned objectives, it is then assumed one ~~do~~ does not need to define more realistic aerosol models for every single OMI pixel. With $g = 0.7$, the Henyey-Greenstein function is known to be smooth and reproduce the Mie scattering functions reasonably well for most of aerosol types, in particular for spherical particles (e.g. nitrate, sulfate) (Dubovik et al., 2002). Such an approach is used for the preparation of the operational

ALH retrieval algorithms for Sentinel-4 and Sentinel-5 Precursor (Leitão et al., 2010; Sanders et al., 2015; Colosimo et al., 2016; Nanda et al., 2017), and for various explicit aerosol corrections in the AMF calculation when retrieving trace gases, such as tropospheric NO_2, over urban and industrial areas dominated by anthropogenic pollution, for example in east China (Spada et al., 2006; Wagner et al., 2007; Castellanos et al., 2015; Vlemmix et al., 2010). The potential impact of the modeled scattering phase discussion is kept in mind and further discussed in Sect. 4.4. But reperforming the whole NN training process with more complex particle shape models is computationally very demanding and beyond the scope of this paper. Instead, more elements on specific error analysis are further discussed in Sect. 4.

Maximum seasonal differences between the LIdar climatology of vertical Aerosol Structure for space-based lidar simulation (LIVAS) and 3-year OMI ALH, over cloud-free scenes in north-east Asia with MODIS $\tau(550\,\mathrm{m}) \geq 1.0$, are in the range of 180–800 m (Amiridis et al., 2015; Chimot et al., 2017). the extended previous sensitive study has shown the following: a) Due to the nature of the $O_2{-}O_2$ spectral band, a minimum particle load (i.e. $\tau(550\mathrm{nm}) = 0.5$) is required to be able to exploit the aerosol signal as, below this threshold, low amounts of aerosols have negligible impacts on $N^{\mathrm{s}}_{\mathrm{O_2-O_2}}$ shielding and lead to high ALH bias; b) The aerosol model assumptions are the most critical, in particular ω_0, as they may affect ALH retrieval uncertainty up to 660 m; c) In addition, potential aerosol residuals in the prior surface albedo may impact up to 200 m; ed) An accuracy of 0.2 is required on prior $\tau(550\mathrm{nm})$ to limit ALH bias close to zero when $\tau(550\mathrm{nm}) \geq 1.0$, and below 500 m for $\tau(550\mathrm{nm})$ values close to 0.6.

2.3 The CALIOP and MODIS aerosol products

CALIOP sensor is a standard dual-wavelength elastically backscattered lidar on board the CALIPSO satellite platform, flying since 2006. Equipped with a depolarization channel at 532 nm, it probes the aerosol and cloud vertical layers, from the surface to 40 km above sea level, with a high vertical resolution (Winker et al., 2009). Level 1 scientific data products, distributed by the Atmospheric Science Data Center (ASDC) of NASA, include the lidar calibrated and ~~geolocated~~ geo-located measurements of high-resolution vertical profiles (between 30 and 60 m in the troposphere) of the aerosol and cloud attenuated backscatter coefficients at 532 and 1064 nm with horizontal resolutions of 1/3 km, 1 km and 5 km (Winker et al., 2009).

The CALIOP aerosol level 2 (L2) product contains the retrieved aerosol backscatter and extinction coefficient profiles at 532 and 1064 nm, for each identified and well located aerosol layer, at 5 km horizontal resolution. These retrievals are performed after calibration, range correction, feature detection and classification, and assumptions on lidar extinction-to-backscattering ratio (Winker et al., 2009; Young and Vaughan, 2009).

The MODIS spectrometer was launched on the NASA EOS Aqua platform in May 2002, and has been delivering continuous images of the Earth in the visible, solar and thermal infrared approximately 15 min prior to OMI. The considered MODIS Aqua L2 aerosol product is the collection 6 of MYD04_L2, based on the Dark Target (DT) and Deep Blue (DB) algorithms with a high enough quality assurance flag and an improved calibration of the instrument (Levy et al., 2013). While the MODIS measurement is acquired at the resolution of 1 km, the used MODIS aerosol $\tau(550\mathrm{nm})$ is at 10 $\mathrm{km} \times 10\,\mathrm{km}$, relatively close to the OMI nadir spatial resolution. The expected uncertainties of MODIS $\tau(550\mathrm{nm})$ are about $\pm 0.05 + 15\,\%$ over land for DT (Levy et al., 2013), and about ± 0.03 on average for DB (Sayer et al., 2013).

3 Case studies: results and discussion

3.1 Methodology

OMI ALH retrievals are here obtained using MODIS L2 aerosol ~~$\tau(550\text{nm})$~~ $\tau(550nm)$ from the combined DT DB product as prior input, collocated within a distance of 15 km and where ~~$\tau(550\text{nm}) \geq 0.55$~~ $\tau(550nm) \geq 0.55$ (cf. Sect. 2.2). Mitigating the probability of cloud contamination within the OMI pixel is one of the first criteria for a successful ALH retrieval. For that purpose, we rely on the availability of the MODIS aerosol product with the highest quality assurance flag ensuring that MODIS Aqua ~~$\tau(550\text{nm})$~~ $\tau(550nm)$ is exclusively estimated when a sufficient high amount of cloud-free sub-pixels is available (i.e. at the MODIS measurement resolution of 1 km) (Levy et al., 2013). However, since this may be not completely representative of the atmospheric situation of the OMI pixel, two thresholds are added for each collocated OMI-MODIS pixel: the geometric MODIS cloud fraction to be smaller than 0.1, and the effective OMI cloud fraction lower than 0.2. For this last parameter, it was shown that values higher than 0.3 are generally likely contaminated by clouds while values between 0.1 and 0.2 may be cloud-free but contain a substantial amount of very scattering particles enhancing then the scene brightness (Boersma et al., 2011; Chimot et al., 2016).

The ALH retrievals are applied to the OMI DOAS O_2-O_2 observations, available in the last reprocessed OMCLDO2 product version (Acarreta et al., 2004; Veefkind et al., 2016). A temperature correction is taken into account on the $N^{\text{s}}_{O_2-O_2}$ variable, using the information available in the OMCLDO2 product which is itself based on the temperature profiles of the National Centers for Environmental Prediction (NCEP) analysis data (Veefkind et al., 2016).

The selected case studies include 1) urban and industrial aerosol pollution over east China during three days between October and November 2006, 2) large wildfire episodes in South-America in August 2006 and September 2007, and in east Russia in August 2010 and June 2012, and 3) a Saharan dust transport over sea in June 2012. OMI ALH retrievals are compared with collocated CALIOP products within a distance of ~~50~~ 50-100 km for the cases over east China and South-America, 300 km for ~~west Sahara and~~ east Russia. The larger OMI-CALIOP distance over these two last regions is due to the so-called "row anomaly" which has been significantly perturbing OMI measurements of the Earth-shine radiance at all the wavelengths since 2009. This leads to a reduced number of valid OMI ground-pixels close to the CALIOP track. Details are given at http://www.knmi.nl/omi/research/product/rowanomaly-background.php.

For each study case, the most likely suitable NN algorithm (see Sect. 2.2) is selected by hand. We decided to rely on 1) the OMI UV aerosol absorbing index (UVAI) and 2) their well known absorbing properties (according to the literature) in the visible spectral range in order to approximate the assumption on aerosol ω_0 at the visible (460-490 nm) spectral wavelengths. OMI UVAI is derived by the OMI near-UV aerosol algorithm (OMAERUV) in the 330-388 nm spectral band (Torres et al., 2007). It allows to detect and distinguish UV absorbing from scattering aerosols through the measured change of spectral contrast, with respect to a pure Rayleigh atmosphere. Weakly absorbing or large non-absorbing particles are associated with near-zero or negative UVAI values. A threshold of 1 on UVAI is then specified to detect absorbing particles in the UV and then potentially in the visible.

3.2 Urban aerosol pollution

Fossil-fuel combustion is the main source of air pollution in the large urban and industrialized area of east China. With decreasing temperatures in autumn, coal-burning power plant activity is increased due to a higher energy consumption of heating systems. Consequently, excessive amounts of aerosol particles and their precursors are emitted (Chameides et al., 1999). Moreover, crop residue burning in the agricultural areas of eastern Asia may enhance aerosol concentrations (Xue et al., 2014). Mineral dust particles, from the Taklimakan and Gobi deserts between middle of spring and end of autumn, are transported through westerly winds (Eck et al., 2005; Proestakis et al., 2017). Collectively, the mix of all these pollutants contributes to the formation of regional brown hazes greatly threatening public health, over the North China Plain (NCP) during the dry season (from October to March). They have been frequently detected by satellite and ground-based observations (Ma et al., 2010).

Three typical days between October and November 2006 in east China were selected to illustrate the performance of the NN algorithm over scenes with strong urban aerosol pollution: day 1 of 2006.10.02, day 2 of 2006.10.06 and day 3 of 2006.11.01. As illustrated by the maps in Fig. 1, these days are characterized by high τ values over land as shown by MODIS Aqua: $\tau(550\text{nm})$ in the range of 0.5-1.6 in October 2006, and 0.5-1.3 in November 2006. Lin et al. (2015) estimated ω_0 values in summer (and likely beginning of autumn) in the range of 0.94-0.96 in the visible. This is likely a consequence of lower black carbon particle amounts at that time (compared to winter and spring) and a high dominance of anthropogenic particles such as nitrate and sulfate. These particles may also be mixed, in parts, with desert dust. Consistently, OMI UVAI depicts for the selected days values lower than or close to 1 (see Fig. 1). Therefore, we use the NN algorithm trained with $\omega_0 = 0.95$ assuming low abundance of ~~Uv and visible~~ UV and visible absorbing particles.

Figure 2 depicts the spatial distribution of retrieved OMI ALH for all the selected collocated OMI-MODIS pixels, with a variability between 0.5-3 km. The CALIPSO suborbital tracks were mostly located inland in day 1 and 3, and between inland and over sea in day 2 (cf. Fig 1 and Fig. 2). The aerosol layers in the CALIOP L2 product, based on the total backscatter coefficients (532 nm), are generally located between the surface and 1.5 km height (see Fig. 3). Maximum top heights do not exceed 2 km on 2006.10.06, and 3 km on the two other days. Collocated OMI ALH are mostly located in the middle aerosol layers, and rarely exceed the top and bottom layer limits (see Fig. 2). Overall, for the 3 selected days, the OMI NN retrievals reproduce the spatial CALIOP L2 patterns. Especially, on 2006.10.02, OMI ALH remains relatively stable at the average altitude of 1 km, within the CALIOP L2 aerosol layers (see Fig. 3a). Only at the latitude 36.5° N, both products simultaneously show an increased altitude close to 3 km. On the two other selected days, OMI ALH and CALIOP L2 show simultaneously descending slopes from South to North: a slope of about 2 km over 2.5° latitude on 2006.10.06, and around 1.5 km over 8° latitude on 2006.11.01 (see Fig. 3b and Fig. 3c).

An equivalent CALIOP L2 ALH can be derived by calculating an aerosol extinction weighted average altitude as follows:

$$\mathrm{ALH(CALIOPL2)} = \frac{\sum_{\mathrm{l}} h(l)\sigma(l)}{\sum_{\mathrm{l}} \sigma(l)}. \quad (1)$$

with $\sigma(l)$ the CALIOP aerosol extinction (532 nm) of the vertical layer l defined by its mid-altitude $h(l)$.

In Figure 4, root-mean-square deviation (RMSD) between OMI and CALIOP L2 ALH lies in the range of 462-648 m when the maximum distance between the selected OMI and CALIOP ground pixels is lower than 50 km and with collocated MODIS $\tau(550\mathrm{nm}) \geq 0.55$ (see Fig. 3). Associated bias values (i.e. average difference between OMI and CALIOP ALH per day) are between -86 and -128 m. These results significantly deteriorate, firstly when specifying a lower threshold on collocated MODIS $\tau(550\mathrm{nm})$ (e.g. RMSD $\geq$ 1000 m with all MODIS $\tau(550\mathrm{nm})$ values included), and secondly with a more flexible distance criterion (e.g. RMSD in the range of 594-888 m with a maximum distance of 500 km between the selected OMI and CALIOP ground pixels). The relatively low impact, noticed here, on the distance between OMI and CALIOP pixels is probably related to the large spatial extent of aerosol plumes and their relative spatial homogeneity. The impact of distance between collocated OMI-CALIOP pixels would be more detrimental over scenes with smaller and/or more heterogeneous plumes. Figure. 5 shows the 1-to-1 comparison between OMI and CALIOP L2 ALH within a distance of 50 km per case study and as a function of associated MODIS $\tau(550\mathrm{nm})$. The correlation coefficient (R) between OMI and CALIOP ALH varies per day, between 0.4 and 0.6 for all scenes with MODIS $\tau(550\mathrm{nm}) \geq 0.55$.

3.3 Smoke and absorbing aerosol pollution from biomass-burning

Intensive biomass burning releases large amounts of carbonaceous and black carbon aerosols. The resulting dense smoke layers have a predominance of fine and strongly light absorbing particles, especially in both the UV and visible visible spectral range. Combined with large τ values, this yields large light extinction and Angstrom exponent (≥ 1.5) (Torres et al., 2013; Wu et al., 2014). Figure 6 shows the location and associated MODIS $\tau(550\mathrm{nm})$ and OMI UVAI values for the selected biomass burning episodes: the two first events are over South-America on 2006.08.24 and 2007.09.30; the two last events are over east Russia on 2010.08.08 and 2012.06.23. Due to the very high load of absorbing particles with MODIS $\tau(550\mathrm{nm} \geq 1.1)$, OMI UVAI values are generally higher than 2 and can locally reach 4 suggesting then the use of the NN algorithm trained with $\omega_0 = 0.9$ (cf. Fig. 6).

Several studies have identified loss of sensitivity of CALIOP attenuated backscatter profile measurements at 532 nm over scenes with dense smoke layers, such as over Canadian boreal and Amazonian fire events (Kacenelenbogen et al., 2011; Torres et al., 2013; Wu et al., 2014). Light extinction due to these layers is much larger at 532 nm than at 1064 nm (Pueschel and Livingston, 1990). Since CALIOP does not directly measure the aerosol backscattering but the attenuated backscattering, the range-dependent reduction in CALIOP LIDAR signals due to attenuation occurs more rapidly in the short wavelengths. Therefore, over scenes with heavy smoke particle loads, the attenuated backscatter coefficients (532 nm) in the lower part of the aerosol layer fall below the CALIOP's detection threshold, preventing the identification of the full vertical extent of the aerosol layers (from the top to the bottom). Being a downlooking observation lidar system, CALIOP tends then to mostly detect the top height compared to the base height of the aerosol layer as the laser's energy undergoes substantial attenuation when the beam travels through an optically thick layer (Vaughan et al., 2005; Kim et al., 2013). Therefore, the identified layers that are fully attenuated at 532 nm, in the L1 product, are filtered out in the L2 product. As a consequence of this filtering, CALIOP τ of smoke layers are generally underestimated due to an overestimation of the layer base altitude (Wu et al., 2014; Kim et al., 2013).

Figure 7 ~~depict~~ depicts an example of the loss of sensitivity for a biomass burning case in South-America. The CALIOP aerosol total backscatter (532 nm) and backscatter (1064 nm) coefficients in the L2 product mostly show the top layer of carbonaceous aerosols in the range of 3-4 km altitude with maximum thickness of 1 km, between 14° S and 11° S (see Fig. 7a and 7b). We found that the layers located below are flagged as totally attenuated at the wavelength of 532 nm, according to the CALIOP vertical feature mask. On the northernmost end of the detected plume, the aerosol load is around 2 km height. On the contrary, the CALIOP L1 attenuated backscatter (1064 nm) profile detects an aerosol layer between the surface and 1.5 km, at the latitudes 11-14° S, not visible the CALIOP L1 total attenuated backscatter (532 nm) profile, (see Fig. 7c and 7d) likely due to a better sensitivity of this channel to the particles located close to the surface.

The case of 2006.08.24 over South-America shows the retrieved OMI ALH being well located, i.e. below the first elevated aerosol layer (at about 3 km) and at the top of the second aerosol layer, close to the surface (see Fig. 7d). Contrary to the CALIPSO L1 measurement (532 nm), our retrievals based on OMI visible measurements are not restricted to the top of the smoke or absorbing layer but correctly match with the middle of the layers detected by CALIPSO L1 (1064 nm). The reason that our OMI ALH seems closer to the top of the second layer may be due to a higher aerosol load and/or different layer properties (see. Sect. 4.2).

Figure 8 shows that similar full CALIOP attenuation processes occur with the other selected biomass burning cases. The CALIOP L1 total attenuated backscatter (532 nm) vertical profiles mostly correlate with the top of the detected aerosol layers, while the CALIOP L1 attenuated backscatter (1064 nm) profiles reveal lower layers. On days of 2007.09.30 and 2010.08, the top layers are at elevated altitudes (higher than 3 km), while the lower ones extend from the surface to 1-2 km. On the last day, 2012.06.23, the top layer is lower (between 1 and 2 km). Similarly, all the OMI ALH retrievals are not restricted to the top layers but match, most of the time, with the middle of the layers, sometimes a bit closer to the base of the top layer or the top of the bottom layer. This may depend on the differences in terms of AOD and/or optical properties of each layer (see. Sect. 4.2). In addition, it is worth to noticing: the similar vertical variability (around 500 m) on 2007.09.30 in South-America at the latitudes 8-15° S, and the remarkable descending slope, on 2012.06.23 in east Russia, from North to South at the latitudes 56-58° S present in both OMI ALH and CALIOP L1 products.

Three reasons may explain why OMI visible spectra allow to probe an entire absorbing aerosol layer, contrary to the active satellite visible measurement of CALIOP: 1) OMI measurements rely on the Sun irradiance which is much intenser than the laser pulse of CALIOP, 2) OMI measurements are largely issued from multiple scattering effects occurring at different altitudes allowing then a higher number of photons to reach the lower atmospheric layers, 3) the relative higher signal-to-noise ratio (SNR) of OMI likely allows to better detect and exploit the upcoming signal from smoke layers. On the contrary, contributions of multiple scattering to the CALIOP backscattered signals are lower than single scattering effects within moderately dense dust layer and insignificant within smoke aerosol extinction (Winker, 2003; Liu et al., 2011). Furthermore, retrieving vertical profile of smoke layers from CALIOP requires a high aerosol extinction threshold due to the large associated lidar ratio and thus low SNR (Winker et al., 2013).

3.4 Desert dust transport

The case illustrated in Fig. 9a is a large desert dust plume over ocean surface, with MODIS $\tau(550\mathrm{nm})$ values up to 1.1, released from the Sahara desert and being transported through westerly winds along the African coast. It occurred in summer on ~~2012.06.28~~2007.07.19. Since the Sahara desert is the most important source of mineral particles, associated dust aerosols include hematite and other iron oxides. Spectrally, desert dust is a UV-absorbing particle but quite highly scattering in the visible (contrary to smoke) and longer wavelengths, leading to the appearance of relatively bright plumes (light brown) over the dark marine surface from satellite point of view. The NN algorithm trained with aerosol $\omega_0 = 0.95$ is therefore used here.

The vertical profile of CALIOP L2 aerosol total backscatter (532 nm) shows elevated elevated layers, ranging from 1-2 km at 15° S to ~~3-4~~ 3-6 km at 23° S (see Fig. 9b). Such a slope likely results from large-scale circulation governed by subtropical subsidence of the Intertropical Convergence Zone's northern branch, dry air from the desert, and the Saharan intense sensible heating effect perturbing the temperature inversion layers and thus creating convection uplifting dust from the surface (Prospero and Carlson, 1980). Generally, the OMI ALH results are consistent with CALIOP observations, with elevated values lying between 2 km and ~~4~~ 7 km. ~~Average OMI ALH is about 2.5 which is then~~ They are mostly located in the middle of the large uplifted dust plume from south to north. The ~~median~~ average difference between OMI and CALIOP L2 ALH, collocated within a distance of ~~200~~ 100 km, is ~~-557.8~~ -350 m. ~~The standard deviations is however~~ However, OMI ALH depicts significant variabilities compared to CALIOP ALH. The standard deviation of the related differences is therefore quite large, about ~~1.5~~ 2.1 km.

Several elements likely contribute to the difficulties encountered in this case study. ~~Due to the well developed row anomaly (see. Sect. 3.1), selected OMI pixels are quite distant from the CALIPSO track. As analyzed in Sect. 3.2, large distance can significantly deteriorate the score of the ALH comparisons depending on the aerosol properties, the layer horizontal extension and its homogeneity. Furthermore, desert~~ Desert dust particles can be relatively coarse (thus low α value) and are irregularly shaped ~~. Their optical modeling~~ (i.e. non-spherical). Their optical modelling in the NN training dataset regarding their assumed size and the employed phase function model (cf. Sect. 2.2) may contribute to the higher ALH uncertainties than in urban cases of Sect. 3.2 (see further discussions in Sect. 4.3 and 4.4).

4 Specific error analysis

The analyzed OMI ALH in Sect. 3 may include uncertainties due to assumptions made on the aerosol models used in the NN training dataset. The following sub-sections focus on some specific uncertainty sources that are relevant for these specific case studies. They provide further detailed error analysis and are complementary to the evaluations performed in (Chimot et al., 2017). Most of these analyses are based on synthetic scenarios. Simulations are performed in a similar way as in the NN training dataset (cf. Sect. 2.2). No bias is introduced in the geophysical parameters such as surface, temperature profile and atmospheric trace gases. The true prior aerosol ~~$\tau(550\mathrm{nm}$~~ $\tau(550\mathrm{nm})$ value is given for all the retrievals. Aerosols are assumed to cover the full ground-pixel. The key analyzed variable is the aerosol layer pressure (ALP) which corresponds to ALH expressed in hPa in order to be consistent with all the input parameter specifications (e.g. vertical grid) in the radiative transfer simulations.

4.1 Aerosol single scattering albedo

Aerosol ω_0 represents the scattering vs. absorption efficiency of the particles, and threfore directly drives the magnitude of the applied shielding effect on the O_2-O_2 dimers (Chimot et al., 2016). An overestimated ω_0, in the training database, directly leads to an overestimation of ALH (or underestimation of ALP) as the measured $N^{s}_{O_2-O_2}$ is lower (i.e. stronger shielding) than expected if one would know the true extinction profile and assume a biased ω_0 (Chimot et al., 2017).

Dense smoke layers from wildfires, such as those analyzed in Sect. 3.2, may contain particles that are more absorbing ~~that~~ than the assumed aerosol model. Figure 10 illustrates the impact of particles with $\omega_0 = 0.8$ while the NN algorithm trained with $\omega_0 = 0.9$ is used (same as in Sect. 3.2). No errors are introduced in all the other geophysical parameters. The resulting ALP values are overestimated with a bias up to 100 hPa (around 900 m) for scenes with $\tau(550\mathrm{nm})$ in the range of 0.5-0.9. ALP biases are almost null over scenes with higher aerosol load as the shielding effect due to the already high amount of particles clearly dominates over their optical properties, and thus regardless ω_0 assumptions. These results are in line with those estimated from the use of the NN algorithm trained with $\omega_0 = 0.95$ in Chimot et al. (2017).

4.2 Aerosol vertical distribution

Due to the specific limitations of passive satellite sensor, the OMI ALH ~~retrievals~~ retrieval summarizes in a single scalar value the description of the aerosol extinction profile assuming a specific profile shape. However, aerosol profiles in the observed scene may considerably deviate from this simplified profile description. It is then legitimate to ask the meaning of the retrieved ALH. As explained in Sect. 2, the NNs were trained based on a single "box-layer" with a constant geometric thickness of about 1 km (100 hPa exactly), ALP / ALH being then the mid-pressure / mid-altitude of this layer. Several of the analyzed cases in Sect. 3 depict more extended aerosol layers (e.g. up to 3.5 km in Fig. 8b), or 2 separate layers (e.g. Fig. 7b).

Figure 11 illustrates the retrievals in a case of an extended aerosol layer: thickness of 300 hPa, located between 700 hPa and 1000 hPa. The derived ALP values are close to 850 hPa for scenes with $\tau(550\mathrm{nm}) \geq 0.5$, which corresponds then to the mid-level of the simulated layer. This result may be understood as the true aerosol vertical extinction profile is lower than the assumption. The retrieval reaches then the average altitude where most of the O_2-O_2 is actually shielded.

In Figure 12, ALP is retrieved when 2 separate aerosol layers with same thickness (i.e. 100 hPa) are simulated: an elevated one between 600 hPa and 700 hPa, a lower one between 900 and 1000 hPa. Assuming that both layers have same optical properties, ALP is retrieved close to 800 hPa for $\tau(550\mathrm{nm}) \geq 0.5$ (cf. Fig. 12a). Here, the retrieval corresponds to the average height of both layers. However, when one of these layers has a higher aerosol load (i.e. a higher value for $\tau(550\mathrm{nm})$), the retrieval is: close to the optically thicker aerosol layer for total $\tau(550\mathrm{nm})$ in the range of 0.-1.6, and reach the average height (i.e. 850 hPa) for total $\tau(550\mathrm{nm}) \geq 1.6$. This demonstrates the sensitivity of the retrieval to the extinction properties of the particles and its vertical distribution driving the location where most of the O_2-O_2 dimers are shielded. As a consequence, the retrieved ALP / ALH actually represents a weighted average of the actual aerosol vertical distribution, the weights being the ~~vertical extinction values~~ extinction values distributed along the vertical atmospheric layers.

4.3 Aerosol size

Within the Henyey-Greensteing phase function model, particle size is primarily governed by α which describes the spectral variation of the aerosol load τ. While the NNs were trained for fine particles emitted from anthropogenic activities such as power plants and vehicles (i.e. $\alpha = 1.5$), other particles such as dust can be coarser.

Figure 13 depicts the ALP retrievals assuming scattering particles with $\omega_0 = 0.95$ (same as in Sect. 3.4) but with different α values: 1.5 (consistent with the training dataset) and 0.5. Overestimating α (i.e. underestimating particle size) leads to a increase (decrease) of retrieved ALP (ALH). This is because coarser particles generally extend the length of the average light path, due to reduced multiple scattering, lower the $O_2{-}O_2$ shielding, and thus increases the measured $N^{s}_{O_2-O_2}$ as shown in Chimot et al. (2016). The ALP change is nevertheless about 25 hPa.

4.4 Scattering phase function

~~Modeling~~ Modelling the aerosol scattering phase function requires not only precise information on their size and optical properties, but also their shape and the phase function ~~modeling~~ modelling theory itself. As an example, optical ~~modeling~~ modelling of desert dust can, for some applications, be done using Mie theory which is mostly valid for homogeneous and spherical particles whereas for other applications one could better consider alternative spheroids or T-matrix/Geometric Optics traditionally used for non-spherical particles (de Graaf et al., 2007; Xu et al., 2017).

For reasons explained in Sect. 2.2, the Henyey-Greenstein was employed in the NN training database. This may lead to some errors in ALH / ALP retrievals due to inaccurate scattering angular dependence depending on the particle type and the assumed g parameter. The shape of the phase function is parameterized by g in Henyey-Greenstein ~~modeling~~modelling which reproduces well the Mie scattering function and thus spherical particles. In Chimot et al. (2016), we demonstrated that bias on ALP does not exceed 50 hPa for a typical uncertainty of 0.1 on g over scenes with $\tau(550\mathrm{nm}) \geq 0.5$, assuming no additional bias on α or ω_0. Comparison between Mie and Henyey-Greenstein ~~modeling~~ modelling would mix errors caused by these three parameters altogether, which would then make complex to identify the actual error source. Colosimo et al. (2016); Sanders et al. (2015) show with simulation studies comparing phase function models, although in different spectral bands, that using a scattering layer with constant particle extinction coefficient does reasonably well without additional biases than those analyzed in the previous sections.

Pure desert dust particles are known to be irregularly shaped, and thus the use of the Henyey-Greenstein forward model may be innapropriate in Sect.3.3 and Fig.9. Furthermore, by using a prior τ parameter from MODIS, that may also be derived from an inaccurate and different model, can add some inconsistencies in the OMI ALH retrieval. This may explain in part the larger uncertainties found in Sect.3.3. In further steps, to confirm the real performances of ALH retrievals over a long-time series of OMI measurements and/or a potential implementation in the OMI processing chain, new NN algorithms should be designed and trained with a larger dataset that includes accurate aerosol parameters (size and ω_0) combined with different detailed models of the phase function. Each of these algorithms should be evaluated on a high number of specific observations to conclude on the exact aerosol model type to be assumed for the OMI visible spectral measurements.

4.5 Cloud contamination

When backscattered solar light measurements from UV-vis passive satellite sensors are exploited, detecting cloud-free pixels is one of the most crucial pre-requisite for aerosol retrievals. In spite of a strict cloud-filtering applied in Sect. 3.1, some small cloud residuals may remain in the analyzed scenes, especially over biomass burning episodes where the distinction of dense smoke particles and small cloud layers can be difficult.

Presence of cloud layers have similar effects as aerosols on the OMI visible measurements and the $O_2{-}O_2$ molecules although associated optical thickness are an order of magnitude higher. In Figure 14, cloud layers were added to an aerosol layer located between 700 hPa and 800 hPa. Clouds were simulated as an opaque Lambertian bright layer with an albedo of 0.8 and different effective cloud pressure and fraction values. Such a model is similar to what is employed in the OMCLDO2 algorithm to detect and characterize the presence of clouds within the OMI pixel or to implicitely correct of aerosol effect in trace gas retrievals (Acarreta et al., 2004; Veefkind et al., 2016; Boersma et al., 2011; Chimot et al., 2016). For reminder, it has to be noticed that aerosols are assumed to cover the whole scene in the simulations.

Figure 14 shows that the impact on the ALP retrieval strongly depends on the cloud altitude. If the aerosol layer is located below a cloud with an effective fraction of 0.3, the ALP is strongly biased low (i.e. ALH high) for $\tau(550\mathrm{nm}) \leq 0.8$, while it tends towards the effective cloud pressure for $\tau(550\mathrm{nm}) \geq 0.8$ (cf. Fig. 14c). Such a behavior may be explained by the high $O_2{-}O_2$ shielding caused by the clouds, much higher than what is anticipated by the retrieval algorithm through the given aerosol $\tau(550\mathrm{nm})$. Especially over scenes with a small aerosol load, the assumed optical thickness of the scene is too low to match with the strongly reduced $N^{\mathrm{s}}_{\mathrm{O_2-O_2}}$ measurement. Moreover, the opaque and bright cloud shields part of the scattering layer located below and dominates over the aerosol signal. The retrieval compensates then with a strongly reduced ALP value. When a high aerosol load (both in the scene and in the prior information) roughly corresponds to the optical thickness of the scene, the ALP represents the altitude where most of the $O_2{-}O_2$ shielding occurs: i.e. at the cloud level. This last effect is also visualised in Sanders et al. (2015) with an optically thick aerosol layer and a cirrus above it, although a different spectral band, in the near infrared, is employed

On the contrary, if aerosols are located above the cloud with an effective fraction of 0.3, retrieved ALP is located between both layers (cf. Fig. 14a). Part of the cloud signal is attenuated this time. Similarly to Sect. 4.2, ALP likely represents a weighted average of the extinction vertical profile. This average is not only weighted by the aerosol properties and the cloud altitude but also by the effective cloud fraction. In the presence of a reduced effective cloud fraction (0.1 instead of 0.3), the estimated ALP is lower (decrease of $40\ \mathrm{hPa}$), close to the base height of the aerosol layer.

5 Conclusions

Following the study of Chimot et al. (2017), aerosol layer heights (ALH) were retrieved from OMI cloud-free pixels using the $O_2{-}O_2$ visible absorption band at 477 nm, based on a neural network approach. The physical principle relies on the dependency of the shielding of the $O_2{-}O_2$ dimers on the aerosol height. Three days with urban and industrial pollution episodes in east China, four days with widespread biomass burning events in South-America and Russia and one day of a

Saharan dust plume transport event over ocean were studied in detail. The goal was to evaluate the OMI ALH spatial patterns over case studies. Prior aerosol optical thickness $\tau(550\text{nm})$ information were used from collocated MODIS L2 product (Dark target Deep Blue algorithms). The retrievals were compared with CALIOP along-track product. The selection of events largely depends on the availability of coinciding OMI and CALIOP data over relevant cases.

Good agreement was found between OMI and CALIOP ALH, where the latter was derived from the level 2 (L2) aerosol extinction profile, over urban and industrial pollution episodes: we find root-mean-square deviation in the range of 462-648 m for distances between OMI and CALIOP ground-pixels smaller than 50 km and with collocated MODIS $\tau(550\text{nm}) \geq 0.55$. Similar spatial patterns are also observed between both sensors. Carbonaceous and black carbon particles within dense smoke layers over biomass burning events strongly attenuate the CALIOP backscatter signal (532 nm). As attenuated backscatter profiles decrease more rapidly in the short than in the long wavelengths, only CALIOP L1 measurements (1064 nm) allow to probe the entire vertical extent of smoke aerosol layers. OMI ALH retrievals match well with these last CALIOP measurements. The higher sensitivity of visible spectral measurements acquired by passive satellite sensors, such as OMI, to capture information from lower altitudes of an optically thick absorbing layer is probably due to the observation of multiple scattered lights from different atmospheric altitudes combined with a ~~high~~ higher signal-to-noise ratio than CALIOP. While scattering leads to a strong reduction of the active signal (i.e. lidar) in penetration depth, this reduction is much lower for a remote sensing sensor using the Solar light source as the fraction of detected photons that reached the lower part of the aerosol layer is considerably higher. Finally, although OMI ALH shows in general consistent results with respect to CALIOP over the transport of the Saharan dust plume over ocean (difference median of -557.8 km), it remains locally limited likely due to ~~1) the large distance between OMI and CALIOP ground-based pixels, and 2) the potential artifacts~~ the potential artefacts due to inaccurate ~~modeling~~ modelling of this particle type in the NN training database, notably regarding its non-spherical and irregular shape and coarse size.

Detailed analyses and discussions on specific error sources confirm that prior assumptions on aerosol optical properties are the key crucial factor affecting the OMI ALH retrieval accuracy over cloud-free scenes. In particular, the combination of aerosol single scattering albedo, particle size and shape, and the angular dependency of the scattering phase function assumptions may impact up to 500 m for each individual parameter. The reason is the direct impact of these variables on the $\mathrm{O_2}-\mathrm{O_2}$ dimers shielding applied by aerosols. Furthermore, a strict cloud filtering is required to distinguish aerosol from cloud effects. The impact of cloud residuals is a function of the cloud coverage and vertical location with respect to the aerosol layer. Finally, the true meaning of the retrieved ALH parameter depends on the actual aerosol vertical distribution. It can be summarized as the weighted average of the optical (or extinction) particle properties along the vertical atmospheric layers, an optically thick (or strongly absorbing) layer having more weights than an optically thin (or highly scattering) particle layer.

Future works should include further comparisons with multiple sensors (satellite, ground-based and airborne), generation of yearly series, trend analysis and then evaluation of aerosol effect correction in support of satellite UV-vis trace gas retrievals (e.g. tropospheric $\mathrm{NO_2}$). The use of satellite $\mathrm{O_2}-\mathrm{O_2}$ visible absorption band should be further studied for aerosol retrievals in addition to the consideration of the more traditional $\mathrm{O_2}$ band in the near infrared as it may bring additional relevant information.

Moreover, expectation for air quality and climate research from a future global OMI ALH product, with a high temporal resolution, should be further investigated, and required improvements should be implemented for an optimal exploitation.

Data availability. All the data results and specific algorithms created in this study are available from the authors upon request. If you are interested to have access to them, please send a message to j.j.chimot@tudelft.nl. The pybrain library code is available at http://pybrain.org/. Finally, The OMCLDO2 dataset is available from the NASA archives: https://disc.gsfc.nasa.gov/uui/datasets/OMCLDO2_003/summary.

Competing interests. The authors declare that they have no conflict of interest.

Acknowledgements. This work was funded by the Netherlands Space Office (NSO) under the OMI contract. The authors thank Piet Stammes from KNMI for the discussions about aerosol modeling and measurements, and Marc Vaughan from NASA for CALIOP aerosol discussions.

References

Acarreta, J. R., de Haan, J. F., and Stammes, P.: Cloud pressure retrieval using the O_2-O_2 absorption band at 477 nm, Journal of Geophysical Research: Atmospheres, 109, n/a–n/a, https://doi.org/10.1029/2003JD003915, http://dx.doi.org/10.1029/2003JD003915, d05204, 2004.

Amiridis, V., Marinou, E., Tsekeri, A., Wandinger, U., Schwarz, A., Giannakaki, E., Mamouri, R., Kokkalis, P., Binietoglou, I., Solomos, S., Herekakis, T., Kazadzis, S., Gerasopoulos, E., Proestakis, E., Kottas, M., Balis, D., Papayannis, A., Kontoes, C., Kourtidis, K., Papagiannopoulos, N., Mona, L., Pappalardo, G., Le Rille, O., and Ansmann, A.: LIVAS: a 3-D multi-wavelength aerosol/cloud database based on CALIPSO and EARLINET, Atmospheric Chemistry and Physics, 15, 7127–7153, https://doi.org/10.5194/acp-15-7127-2015, http://www.atmos-chem-phys.net/15/7127/2015/, 2015.

Barkley, M. P., Kurosu, T. P., Chance, K., De Smedt, I., Van Roozendael, M., Arneth, A., Hagberg, D., and Guenther, A.: Assessing sources of uncertainty in formaldehyde air mass factors over tropical South America: Implications for top-down isoprene emission estimates, Journal of Geophysical Research: Atmospheres, 117, n/a–n/a, https://doi.org/10.1029/2011JD016827, http://dx.doi.org/10.1029/2011JD016827, d13304, 2012.

Boersma, K. F., Eskes, H. J., and Brinksma, E. J.: Error analysis for tropospheric NO2 retrieval from space, Journal of Geophysical Research: Atmospheres, 109, n/a–n/a, https://doi.org/10.1029/2003JD003962, http://dx.doi.org/10.1029/2003JD003962, d04311, 2004.

Boersma, K. F., Eskes, H. J., Dirksen, R. J., van der A, R. J., Veefkind, J. P., Stammes, P., Huijnen, V., Kleipool, Q. L., Sneep, M., Claas, J., Leitao, J., Richter, A., Zhou, Y., and Brunner, D.: An improved tropospheric NO_2 column retrieval algorithm for the Ozone Monitoring Instrument, Atmospheric Measurement Techniques, 4, 1905–1928, https://doi.org/10.5194/amt-4-1905-2011, http://www.atmos-meas-tech.net/4/1905/2011/, 2011.

Castellanos, P., Boersma, K. F., Torres, O., and de Haan, J. F.: OMI tropospheric NO_2 air mass factors over South America: effects of biomass burning aerosols, Atmospheric Measurement Techniques, 8, 3831–3849, https://doi.org/10.5194/amt-8-3831-2015, http://www.atmos-meas-tech.net/8/3831/2015/, 2015.

Chameides, W. L., Yu, H., Liu, S. C., Bergin, M., Zhou, X., Mearns, L., Wang, G., Kiang, C. S., Saylor, R. D., Luo, C., Huang, Y., Steiner, A., and Giorgi, F.: Case study of the effects of atmospheric aerosols and regional haze on agriculture: An opportunity to enhance crop yields in China through emission controls?, Proceedings of the National Academy of Sciences, 96, 13 626–13 633, https://doi.org/10.1073/pnas.96.24.13626, http://www.pnas.org/content/96/24/13626.abstract, 1999.

Chimot, J., Vlemmix, T., Veefkind, J. P., de Haan, J. F., and Levelt, P. F.: Impact of aerosols on the OMI tropospheric NO_2 retrievals over industrialized regions: how accurate is the aerosol correction of cloud-free scenes via a simple cloud model?, Atmospheric Measurement Techniques, 9, 359–382, https://doi.org/10.5194/amt-9-359-2016, http://www.atmos-meas-tech.net/9/359/2016/, 2016.

Chimot, J., Veefkind, J. P., Vlemmix, T., de Haan, J. F., Amiridis, V., Proestakis, E., Marinou, E., and Levelt, P. F.: An exploratory study on the aerosol height retrieval from OMI measurements of the 477 nm O_2-O_2, spectral band using a neural network approach, Atmospheric Measurement Techniques, 10, 783–809, https://doi.org/10.5194/amt-10-783-2017, http://www.atmos-meas-tech.net/10/783/2017/, 2017.

Colosimo, S. F., Natraj, V., Sander, S. P., and Stutz, J.: A sensitivity study on the retrieval of aerosol vertical profiles using the oxygen A-band, Atmospheric Measurement Techniques, 9, 1889–1905, https://doi.org/10.5194/amt-9-1889-2016, http://www.atmos-meas-tech.net/9/1889/2016/, 2016.

Connor, B., Bösch, H., McDuffie, J., Taylor, T., Fu, D., Frankenberg, C., O'Dell, C., Payne, V. H., Gunson, M., Pollock, R., Hobbs, J., Oyafuso, F., and Jiang, Y.: Quantification of uncertainties in OCO-2 measurements of XCO_2: simulations and linear error analysis, At-

mospheric Measurement Techniques, 9, 5227–5238, https://doi.org/10.5194/amt-9-5227-2016, https://www.atmos-meas-tech.net/9/5227/2016/, 2016.

Crisp, D.: Measuring atmospheric carbon dioxide from space with the Orbiting Carbon Observatory-2 (OCO-2), vol. 9607, pp. 9607–9607–7, https://doi.org/10.1117/12.2187291, http://dx.doi.org/10.1117/12.2187291, 2015.

de Graaf, M., Stammes, P., and Aben, E. A. A.: Analysis of reflectance spectra of UV-absorbing aerosol scenes measured by SCIAMACHY, Journal of Geophysical Research: Atmospheres, 112, n/a–n/a, https://doi.org/10.1029/2006JD007249, http://dx.doi.org/10.1029/2006JD007249, d02206, 2007.

de Graaf, M., Tilstra, L. G., Wang, P., and Stammes, P.: Retrieval of the aerosol direct radiative effect over clouds from spaceborne spectrometry, Journal of Geophysical Research: Atmospheres, 117, https://doi.org/10.1029/2011JD017160, http://dx.doi.org/10.1029/2011JD017160, d07207, 2012.

de Haan, J. F.: DISAMAR Algorithm Description and Background Information, Royal Netherlands Meteorological Institute, De Bilt, the Netherlands, 2011.

Ding, S., Wang, J., and Xu, X.: Polarimetric remote sensing in oxygen A and B bands: sensitivity study and information content analysis for vertical profile of aerosols, Atmospheric Measurement Techniques, 9, 2077–2092, https://doi.org/10.5194/amt-9-2077-2016, https://www.atmos-meas-tech.net/9/2077/2016/, 2016.

Dubovik, O., Holben, B., Eck, T. F., Smirnov, A., Kaufman, Y. J., King, M. D., Tanré, D., and Slutsker, I.: Variability of Absorption and Optical Properties of Key Aerosol Types Observed in Worldwide Locations, Journal of the Atmospheric Sciences, 59, 590–608, https://doi.org/10.1175/1520-0469(2002)059<0590:VOAAOP>2.0.CO;2, http://dx.doi.org/10.1175/1520-0469(2002)059<0590:VOAAOP>2.0.CO;2, 2002.

Duncan, B., Prados, A., Lamsal, L., Liu, Y., Streets, D., Gupta, P., Hilsenrath, E., Kahn, R., Nielsen, J., Beyersdorf, A., Burton, S., Fiore, A., Fishman, J., Henze, D., Hostetler, C., Krotkov, N., Lee, P., Lin, M., Pawson, S., Pfister, G., Pickering, K., Pierce, R., Yoshida, Y., and Ziemba, L.: Satellite data of atmospheric pollution for U.S. air quality applications: Examples of applications, summary of data end-user resources, answers to FAQs, and common mistakes to avoid, Atmospheric Environment, 94, 647 – 662, https://doi.org/https://doi.org/10.1016/j.atmosenv.2014.05.061, http://www.sciencedirect.com/science/article/pii/S1352231014004270, 2014.

Eck, T. F., Holben, B. N., Dubovik, O., Smirnov, A., Goloub, P., Chen, H. B., Chatenet, B., Gomes, L., Zhang, X.-Y., Tsay, S.-C., Ji, Q., Giles, D., and Slutsker, I.: Columnar aerosol optical properties at AERONET sites in central eastern Asia and aerosol transport to the tropical mid-Pacific, Journal of Geophysical Research: Atmospheres, 110, n/a–n/a, https://doi.org/10.1029/2004JD005274, http://dx.doi.org/10.1029/2004JD005274, d06202, 2005.

Figueras i Ventura, J. and Russchenberg, H.: Towards a better understanding of the impact of anthropogenic aerosols in the hydrological cycle: IDRA, IRCTR drizzle radar, Physics and Chemistry of the Earth, Parts A/B/C, 34, 88 – 92, https://doi.org/https://doi.org/10.1016/j.pce.2008.02.038, http://www.sciencedirect.com/science/article/pii/S1474706508000594, sustainable Water Solutions, 2009.

Hewson, W., Barkley, M. P., Gonzalez Abad, G., Bösch, H., Kurosu, T., Spurr, R., and Tilstra, L. G.: Development and characterisation of a state-of-the-art GOME-2 formaldehyde air-mass factor algorithm, Atmospheric Measurement Techniques, 8, 4055–4074, https://doi.org/10.5194/amt-8-4055-2015, http://www.atmos-meas-tech.net/8/4055/2015/, 2015.

Hovenier, J. W. and Hage, J. I.: Relations involving the spherical albedo and other photometric quantities of planets with thick atmospheres, , 214, 391–401, http://adsabs.harvard.edu/abs/1989A%26A...214..391H, provided by the SAO/NASA Astrophysics Data System, 1989.

Hsu, N., Herman, J., and Tsay, S.-C.: Radiative impacts from biomass burning in the presence of clouds during boreal spring in southeast Asia, Geophysical Research Letters, 30, https://doi.org/10.1029/2002GL016485, http://dx.doi.org/10.1029/2002GL016485, 1224, 2003.

Hu, H., Hasekamp, O., Butz, A., Galli, A., Landgraf, J., Aan de Brugh, J., Borsdorff, T., Scheepmaker, R., and Aben, I.: The operational methane retrieval algorithm for TROPOMI, Atmospheric Measurement Techniques, 9, 5423–5440, https://doi.org/10.5194/amt-9-5423-2016, https://www.atmos-meas-tech.net/9/5423/2016/, 2016.

Ingmann, I., Veihelmann, B., Langen, J., Lamarre, D., Stark, H., and Bazalgette Courrèges-Lacoste, G.: Requirements for the GMES Atmosphere Service and ESA's implementation concept: Sentinels-4/-5 and -5p, Remote Sensing of Environment, 120, 58 – 69, https://doi.org/https://doi.org/10.1016/j.rse.2012.01.023, http://www.sciencedirect.com/science/article/pii/S0034425712000673, the Sentinel Missions - New Opportunities for Science, 2012.

IPCC: The Core Writing Team Pachauri, R. K. and Meyer, L. A.: Climate Change 2014: Synthesis Report. Contribution of Working Groups I, II and III to the Fifth Assessment Report of the Intergovernmental Panel on Climate Change, IPCC, Geneva, Switzerland, http://www.ipcc.ch/report/ar5/syr/, 2014.

Kacenelenbogen, M., Vaughan, M. A., Redemann, J., Hoff, R. M., Rogers, R. R., Ferrare, R. A., Russell, P. B., Hostetler, C. A., Hair, J. W., and Holben, B. N.: An accuracy assessment of the CALIOP/CALIPSO version 2/version 3 daytime aerosol extinction product based on a detailed multi-sensor, multi-platform case study, Atmospheric Chemistry and Physics, 11, 3981–4000, https://doi.org/10.5194/acp-11-3981-2011, http://www.atmos-chem-phys.net/11/3981/2011/, 2011.

Kim, M.-H., Kim, S.-W., Yoon, S.-C., and Omar, A. H.: Comparison of aerosol optical depth between CALIOP and MODIS-Aqua for CALIOP aerosol subtypes over the ocean, Journal of Geophysical Research: Atmospheres, 118, 13,241–13,252, https://doi.org/10.1002/2013JD019527, http://dx.doi.org/10.1002/2013JD019527, 2013JD019527, 2013.

Kipling, Z., Stier, P., Johnson, C. E., Mann, G. W., Bellouin, N., Bauer, S. E., Bergman, T., Chin, M., Diehl, T., Ghan, S. J., Iversen, T., Kirkevåg, A., Kokkola, H., Liu, X., Luo, G., van Noije, T., Pringle, K. J., von Salzen, K., Schulz, M., Seland, Ø., Skeie, R. B., Takemura, T., Tsigaridis, K., and Zhang, K.: What controls the vertical distribution of aerosol? Relationships between process sensitivity in HadGEM3–UKCA and inter-model variation from AeroCom Phase II, Atmospheric Chemistry and Physics, 16, 2221–2241, https://doi.org/10.5194/acp-16-2221-2016, https://www.atmos-chem-phys.net/16/2221/2016/, 2016.

Koffi, B., Schulz, M., Bréon, F.-M., Griesfeller, J., Winker, D., Balkanski, Y., Bauer, S., Berntsen, T., Chin, M., Collins, W., Dentener, F., Diehl, T., Easter, R., Ghan, S., Ginoux, P., Gong, S., Horowitz, L., Iversen, T., Kirkevåg, A., Koch, D., Krol, M., Myhre, G., Stier, P., and Takemura, T.: Application of the CALIOP layer product to evaluate the vertical distribution of aerosols estimated by global models: AeroCom phase I results, Journal of Geophysical Research: Atmospheres, 117, https://doi.org/10.1029/2011JD016858, http://dx.doi.org/10.1029/2011JD016858, d10201, 2012.

Krotkov, N. A., McClure, B., Dickerson, R. R., Carn, S. A., Li, C., Bhartia, P. K., Yang, K., Krueger, A. J., Li, Z., Levelt, P. F., Chen, H., Wang, P., and Lu, D.: Validation of SO_2 retrievals from the Ozone Monitoring Instrument over NE China, Journal of Geophysical Research: Atmospheres, 113, n/a–n/a, https://doi.org/10.1029/2007JD008818, http://dx.doi.org/10.1029/2007JD008818, d16S40, 2008.

Leitão, J., Richter, A., Vrekoussis, M., Kokhanovsky, A., Zhang, Q. J., Beekmann, M., and Burrows, J. P.: On the improvement of NO_2 satellite retrievals – aerosol impact on the airmass factors, Atmospheric Measurement Techniques, 3, 475–493, https://doi.org/10.5194/amt-3-475-2010, http://www.atmos-meas-tech.net/3/475/2010/, 2010.

Levelt, P. F., Hilsenrath, E., Leppelmeier, G. W., van den Oord, G. H. J., Bhartia, P. K., Tamminen, J., de Haan, J. F., and Veefkind, J. P.: Science Objectives of the Ozone Monitoring Instrument, IEEE Transactions on Geoscience and Remote Sensing, 44, 1199–1208, https://doi.org/10.1109/TGRS.2006.872336, 2006.

Levy, R. C., Mattoo, S., Munchak, L. A., Remer, L. A., Sayer, A. M., Patadia, F., and Hsu, N. C.: The Collection 6 MODIS aerosol products over land and ocean, Atmospheric Measurement Techniques, 6, 2989–3034, https://doi.org/10.5194/amt-6-2989-2013, http://www.atmos-meas-tech.net/6/2989/2013/, 2013.

Lin, J.-T., Liu, M.-Y., Xin, J.-Y., Boersma, K. F., Spurr, R., Martin, R., and Zhang, Q.: Influence of aerosols and surface reflectance on satellite NO_2 retrieval: seasonal and spatial characteristics and implications for NO_x emission constraints, Atmospheric Chemistry and Physics, 15, 11 217–11 241, https://doi.org/10.5194/acp-15-11217-2015, http://www.atmos-chem-phys.net/15/11217/2015/, 2015.

Liu, Z., Winker, D., Omar, A., Vaughan, M., Trepte, C., Hu, Y., Powell, K., Sun, W., and Lin, B.: Effective lidar ratios of dense dust layers over North Africa derived from the {CALIOP} measurements, Journal of Quantitative Spectroscopy and Radiative Transfer, 112, 204 – 213, https://doi.org/https://doi.org/10.1016/j.jqsrt.2010.05.006, http://www.sciencedirect.com/science/article/pii/S0022407310001755, international Symposium on Atmospheric Light Scattering and Remote Sensing (ISALSaRS'09), 2011.

Loeb, N. and Su, W.: Direct Aerosol Radiative Forcing Uncertainty Based on a Radiative Perturbation Analysis, Journal of Climate, 23, 5288–5293, https://doi.org/10.1175/2010JCLI3543.1, https://doi.org/10.1175/2010JCLI3543.1, 2010.

Ma, J., Chen, Y., Wang, W., Yan, P., Liu, H., Yang, S., Hu, Z., and Lelieveld, J.: Strong air pollution causes widespread haze-clouds over China, Journal of Geophysical Research: Atmospheres, 115, n/a–n/a, https://doi.org/10.1029/2009JD013065, http://dx.doi.org/10.1029/2009JD013065, d18204, 2010.

Martin, R.: Satellite remote sensing of surface air quality, Atmospheric Environment, 42, 7823 – 7843, https://doi.org/https://doi.org/10.1016/j.atmosenv.2008.07.018, ttp://www.sciencedirect.com/science/article/pii/S1352231008006328, 2008.

McComiskey, A., Schwartz, S., Schmid, B., Guan, H., Lewis, E., Ricchiazzi, P., and Ogren, J.: Direct aerosol forcing: Calculation from observables and sensitivities to inputs, Journal of Geophysical Research: Atmospheres, 113, https://doi.org/10.1029/2007JD009170, http://dx.doi.org/10.1029/2007JD009170, d09202, 2008.

Nanda, S., de Graaf, M., Sneep, M., de Haan, J. F., Stammes, P., Sanders, A. F. J., Tuinder, O., Veefkind, J. P., and Levelt, P. F.: Error sources in the retrieval of aerosol information over bright surfaces from satellite measurements in the oxygen A-band, Atmospheric Measurement Techniques Discussions, 2017, 1–26, https://doi.org/10.5194/amt-2017-323, https://www.atmos-meas-tech-discuss.net/amt-2017-323/, 2017.

Palancar, G. G., Lefer, B. L., Hall, S. R., Shaw, W. J., Corr, C. A., Herndon, S. C., Slusser, J. R., and Madronich, S.: Effect of aerosols and NO_2 concentration on ultraviolet actinic flux near Mexico City during MILAGRO: measurements and model calculations, Atmospheric Chemistry and Physics, 13, 1011–1022, https://doi.org/10.5194/acp-13-1011-2013, https://www.atmos-chem-phys.net/13/1011/2013/, 2013.

Park, S. S., Kim, J., Lee, H., Torres, O., Lee, K.-M., and Lee, S. D.: Utilization of O_4 slant column density to derive aerosol layer height from a space-borne UV–visible hyperspectral sensor: sensitivity and case study, Atmospheric Chemistry and Physics, 16, 1987–2006, https://doi.org/10.5194/acp-16-1987-2016, http://www.atmos-chem-phys.net/16/1987/2016/, 2016.

Platt, U. and Stutz, J.: Differential Optical Absorption Spectroscopy (DOAS), Principles and Applications, Springer-Verlag Berlin Heidelberg, https://doi.org/10.1007/978-3-540-75776-4, 2008.

Proestakis, E., Amiridis, V., Marinou, E., Georgoulias, A. K., Solomos, S., Kazadzis, S., Chimot, J., Che, H., Alexandri, G., Binietoglou, I., Kourtidis, K. A., de Leeuw, G., and van der A, R. J.: 9-year spatial and temporal evolution of desert dust aerosols over South-East Asia as revealed by CALIOP, Atmospheric Chemistry and Physics Discussions, 2017, 1–35, https://doi.org/10.5194/acp-2017-797, https://www.atmos-chem-phys-discuss.net/acp-2017-797/, 2017.

Prospero, J. and Carlson, N.: Saharan Air Outbreaks Over the Tropical North Atlantic, 119, 677–691, 1980.

Pueschel, R. F. and Livingston, J. M.: Aerosol spectral optical depths: Jet fuel and forest fire smokes, Journal of Geophysical Research: Atmospheres, 95, 22 417–22 422, https://doi.org/10.1029/JD095iD13p22417, http://dx.doi.org/10.1029/JD095iD13p22417, 1990.

Sanders, A. F. J., de Haan, J. F., Sneep, M., Apituley, A., Stammes, P., Vieitez, M. O., Tilstra, L. G., Tuinder, O. N. E., Koning, C. E., and Veefkind, J. P.: Evaluation of the operational Aerosol Layer Height retrieval algorithm for Sentinel-5 Precursor: application to O_2 A band observations from GOME-2A, Atmospheric Measurement Techniques, 8, 4947–4977, https://doi.org/10.5194/amt-8-4947-2015, http://www.atmos-meas-tech.net/8/4947/2015/, 2015.

Sarna, K. and Russchenberg, H. W. J.: Monitoring aerosol–cloud interactions at the CESAR Observatory in the Netherlands, Atmospheric Measurement Techniques, 10, 1987–1997, https://doi.org/10.5194/amt-10-1987-2017, https://www.atmos-meas-tech.net/10/1987/2017/, 2017.

Sayer, A. M., Hsu, N. C., Bettenhausen, C., and Jeong, M.-J.: Validation and uncertainty estimates for MODIS Collection 6 "Deep Blue" aerosol data, Journal of Geophysical Research: Atmospheres, 118, 7864–7872, https://doi.org/10.1002/jgrd.50600, http://dx.doi.org/10.1002/jgrd.50600, 2013.

Spada, F., Krol, M. C., and Stammes, P.: McSCIA: application of the Equivalence Theorem in a Monte Carlo radiative transfer model for spherical shell atmospheres, Atmospheric Chemistry and Physics, 6, 4823–4842, https://doi.org/10.5194/acp-6-4823-2006, http://www.atmos-chem-phys.net/6/4823/2006/, 2006.

Torres, O., Tanskanen, A., Veihelmann, B., Ahn, C., Braak, R., Bhartia, P. K., Veefkind, P., and Levelt, P.: Aerosols and surface UV products from Ozone Monitoring Instrument observations: An overview, Journal of Geophysical Research: Atmospheres, 112, n/a–n/a, https://doi.org/10.1029/2007JD008809, http://dx.doi.org/10.1029/2007JD008809, d24S47, 2007.

Torres, O., Ahn, C., and Chen, Z.: Improvements to the OMI near-UV aerosol algorithm using A-train CALIOP and AIRS observations, Atmospheric Measurement Techniques, 6, 3257–3270, https://doi.org/10.5194/amt-6-3257-2013, http://www.atmos-meas-tech.net/6/3257/2013/, 2013.

Vaughan, M., Winker, D., and Powell, K.: CALIOP Algorithm Theoretical Basis Document - Part 2: Feature Detection and Layer Properties Algorithms, 2005.

Veefkind, J. P., Aben, I., McMullan, K., Förster, H., de Vries, J., Otter, G., Claas, J., Eskes, H. J., de Haan, J. F., Kleipool, Q., van Weele, M., Hasekamp, O., Hoogeveen, R., Landgraf, J., Snel, R., Tol, P., Ingmann, P., Voors, R., Kruizinga, B., Vink, R., Visser, H., and Levelt, P. F.: TROPOMI on the ESA Sentinel-5 Precursor: A GMES mission for global observations of the atmospheric composition for climate, air quality and ozone layer applications, Remote sensing of environment., 120, 70—83, https://doi.org/10.1016/j.rse.2011.09.027, http://dx.doi.org/10.1016/j.rse.2011.09.027, 2012.

Veefkind, J. P., de Haan, J. F., Sneep, M., and Levelt, P. F.: Improvements of the OMI O_2-O_2 Operational Cloud Algorithm and Comparisons with Ground-Based Radar-Lidar Observations, Atmospheric Measurement Techniques Discussions, 2016, 1–28, https://doi.org/10.5194/amt-2016-48, http://www.atmos-meas-tech-discuss.net/amt-2016-48/, 2016.

Vlemmix, T., Piters, A. J. M., Stammes, P., Wang, P., and Levelt, P. F.: Retrieval of tropospheric NO_2 using the MAX-DOAS method combined with relative intensity measurements for aerosol correction, Atmospheric Measurement Techniques, 3, 1287–1305, https://doi.org/10.5194/amt-3-1287-2010, http://www.atmos-meas-tech.net/3/1287/2010/, 2010.

Wagner, T., Burrows, J. P., Deutschmann, T., Dix, B., von Friedeburg, C., Frieß, U., Hendrick, F., Heue, K.-P., Irie, H., Iwabuchi, H., Kanaya, Y., Keller, J., McLinden, C. A., Oetjen, H., Palazzi, E., Petritoli, A., Platt, U., Postylyakov, O., Pukite, J., Richter, A., van Roozendael, M., Rozanov, A., Rozanov, V., Sinreich, R., Sanghavi, S., and Wittrock, F.: Comparison of box-air-mass-factors and radiances for Multiple-Axis Differential Optical Absorption Spectroscopy (MAX-DOAS) geometries calculated from different UV/visible radiative transfer

models, Atmospheric Chemistry and Physics, 7, 1809–1833, https://doi.org/10.5194/acp-7-1809-2007, http://www.atmos-chem-phys.net/7/1809/2007/, 2007.

Wang, P., Tuinder, O. N. E., Tilstra, L. G., de Graaf, M., and Stammes, P.: Interpretation of FRESCO cloud retrievals in case of absorbing aerosol events, Atmospheric Chemistry and Physics, 12, 9057–9077, https://doi.org/10.5194/acp-12-9057-2012, http://www.atmos-chem-phys.net/12/9057/2012/, 2012.

Wilcox, E. M.: Direct and semi-direct radiative forcing of smoke aerosols over clouds, Atmospheric Chemistry and Physics, 12, 139–149, https://doi.org/10.5194/acp-12-139-2012, https://www.atmos-chem-phys.net/12/139/2012/, 2012.

Winker, D.: Accounting for multiple scattering in retrievals from space lidar, in: 12th International Workshop on Lidar Multiple Scattering Experiments, vol. 5059, pp. 128–139, https://doi.org/10.1117/12.512352, http://dx.doi.org/10.1117/12.512352, 2003.

Winker, D., Vaughan, M., Omar, A., Hu, Y., Powell, K., Liu, Z., Hunt, W., and Young, S.: Overview of the CALIPSO Mission and CALIOP Data Processing Algorithms, Journal of Atmospheric and Oceanic Technology, 26, 2310–2323, https://doi.org/10.1175/2009JTECHA1281.1, http://dx.doi.org/10.1175/2009JTECHA1281.1, 2009.

Winker, D. M., Tackett, J. L., Getzewich, B. J., Liu, Z., Vaughan, M. A., and Rogers, R. R.: The global 3-D distribution of tropospheric aerosols as characterized by CALIOP, Atmospheric Chemistry and Physics, 13, 3345–3361, https://doi.org/10.5194/acp-13-3345-2013, https://www.atmos-chem-phys.net/13/3345/2013/, 2013.

Wu, Y., Cordero, L., Gross, B., Moshary, F., and Ahmed, S.: Assessment of {CALIPSO} attenuated backscatter and aerosol retrievals with a combined ground-based multi-wavelength lidar and sunphotometer measurement, Atmospheric Environment, 84, 44 – 53, https://doi.org/https://doi.org/10.1016/j.atmosenv.2013.11.016, http://www.sciencedirect.com/science/article/pii/S1352231013008455, 2014.

Wunch, D., Wennberg, P. O., Osterman, G., Fisher, B., Naylor, B., Roehl, C. M., O'Dell, C., Mandrake, L., Viatte, C., Kiel, M., Griffith, D. W. T., Deutscher, N. M., Velazco, V. A., Notholt, J., Warneke, T., Petri, C., De Maziere, M., Sha, M. K., Sussmann, R., Rettinger, M., Pollard, D., Robinson, J., Morino, I., Uchino, O., Hase, F., Blumenstock, T., Feist, D. G., Arnold, S. G., Strong, K., Mendonca, J., Kivi, R., Heikkinen, P., Iraci, L., Podolske, J., Hillyard, P. W., Kawakami, S., Dubey, M. K., Parker, H. A., Sepulveda, E., García, O. E., Te, Y., Jeseck, P., Gunson, M. R., Crisp, D., and Eldering, A.: Comparisons of the Orbiting Carbon Observatory-2 (OCO-2) $X_{\mathrm{CO_2}}$ measurements with TCCON, Atmospheric Measurement Techniques, 10, 2209–2238, https://doi.org/10.5194/amt-10-2209-2017, https://www.atmos-meas-tech.net/10/2209/2017/, 2017.

Xu, X., Wang, J., Wang, Y., Zeng, J., Torres, O., Yang, Y., Marshak, A., Reid, J., and Miller, S.: Passive remote sensing of altitude and optical depth of dust plumes using the oxygen A and B bands: First results from EPIC/DSCOVR at Lagrange-1 point, Geophysical Research Letters, 44, 7544–7554, https://doi.org/10.1002/2017GL073939, http://dx.doi.org/10.1002/2017GL073939, 2017GL073939, 2017.

Xue, Y., Xu, H., Guang, J., Mei, L., Guo, J., Li, C., Mikusauskas, R., and He, X.: Observation of an agricultural biomass burning in central and east China using merged aerosol optical depth data from multiple satellite missions, International Journal of Remote Sensing, 35, 5971–5983, https://doi.org/10.1080/2150704X.2014.943321, http://dx.doi.org/10.1080/2150704X.2014.943321, 2014.

Young, S. and Vaughan, M.: The Retrieval of Profiles of Particulate Extinction from Cloud-Aerosol Lidar Infrared Pathfinder Satellite Observations (CALIPSO) Data: Algorithm Description, Journal of Atmospheric and Oceanic Technology, 26, 1105–1119, https://doi.org/10.1175/2008JTECHA1221.1, http://dx.doi.org/10.1175/2008JTECHA1221.1, 2009.

Yu, H., Kaufman, Y. J., Chin, M., Feingold, G., Remer, L. A., Anderson, T. L., Balkanski, Y., Bellouin, N., Boucher, O., Christopher, S., DeCola, P., Kahn, R., Koch, D., Loeb, N., Reddy, M. S., Schulz, M., Takemura, T., and Zhou, M.: A review of measurement-based assess-

ments of the aerosol direct radiative effect and forcing, Atmospheric Chemistry and Physics, 6, 613–666, https://doi.org/10.5194/acp-6-613-2006, https://www.atmos-chem-phys.net/6/613/2006/, 2006.

Zarzycki, C. M. and Bond, T. C.: How much can the vertical distribution of black carbon affect its global direct radiative forcing?, Geophysical Research Letters, 37, https://doi.org/10.1029/2010GL044555, http://dx.doi.org/10.1029/2010GL044555, l20807, 2010.

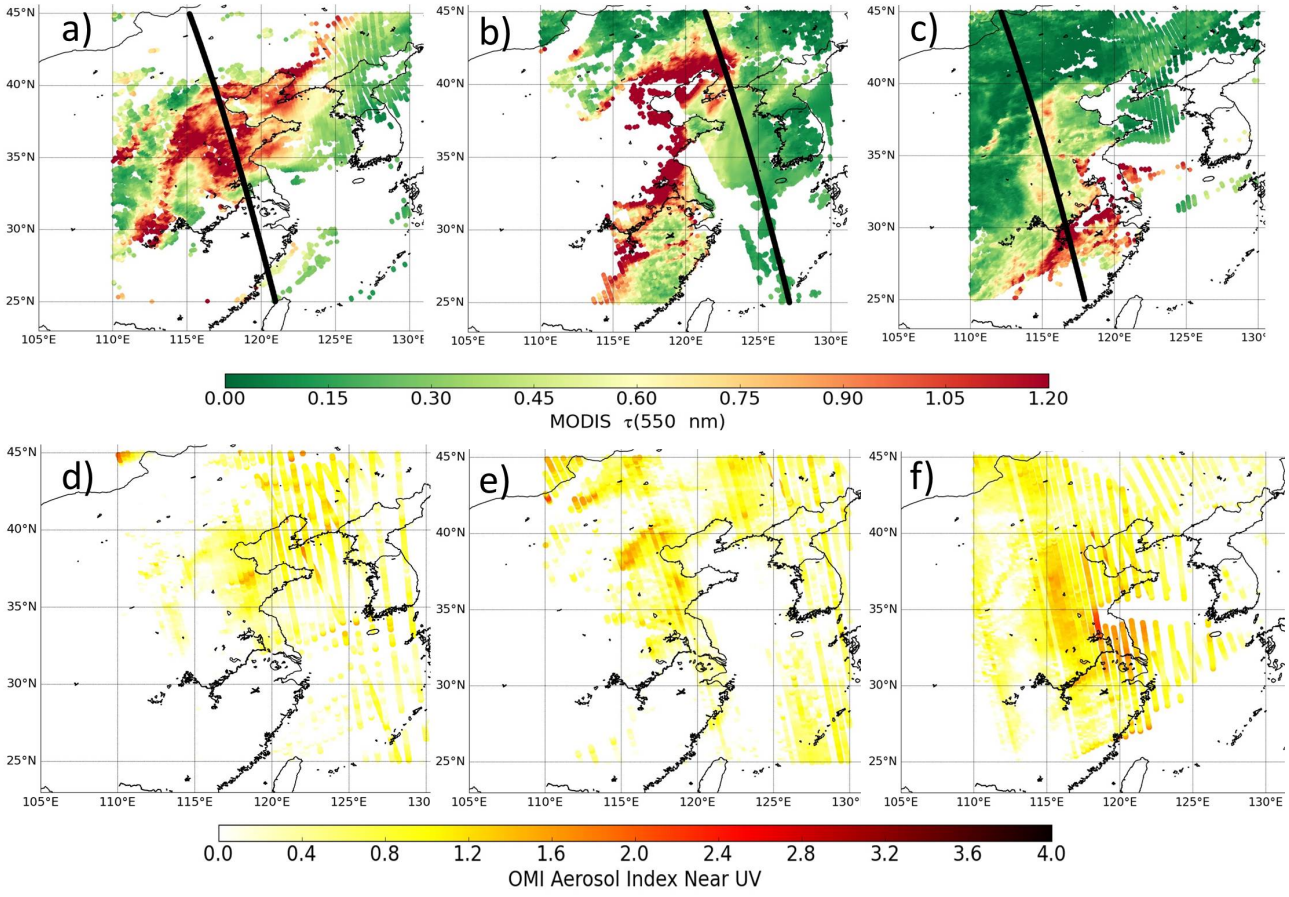

Figure 1. Maps of MODIS Aqua $\tau(550\text{nm})$ from the combined DT and DB Collection 6 (cf. Sect. 2.3), and collocated OMI aerosol index from near UV (UVAI) values (cf. Sect. 3) over cloud-free scenes for the urban and industrialized cases in east China. The dark thick lines represent the track of CALIPSO space-borne sensor over the selected case studies: (**a d**) 2006.10.02, (**b e**) 2006.10.06, (**c f**) 2006.11.01.

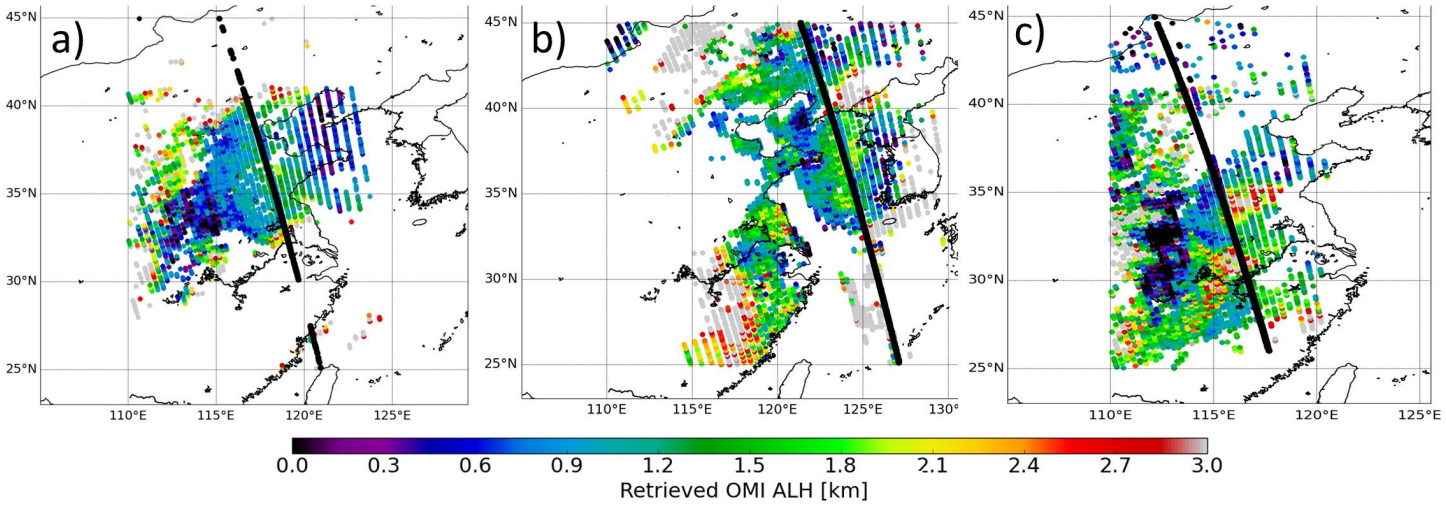

Figure 2. Maps of retrieved OMI aerosol layer height (ALH) from all the cloud-free pixels collocated with MODIS Aqua $\tau(550\text{nm})$ (cf. Fig. 1). The dark thick lines represent the track of CALIPSO space-borne sensor over the selected case studies: (**a**) 2006.10.02, (**b**) 2006.10.06, (**c**) 2006.11.01.

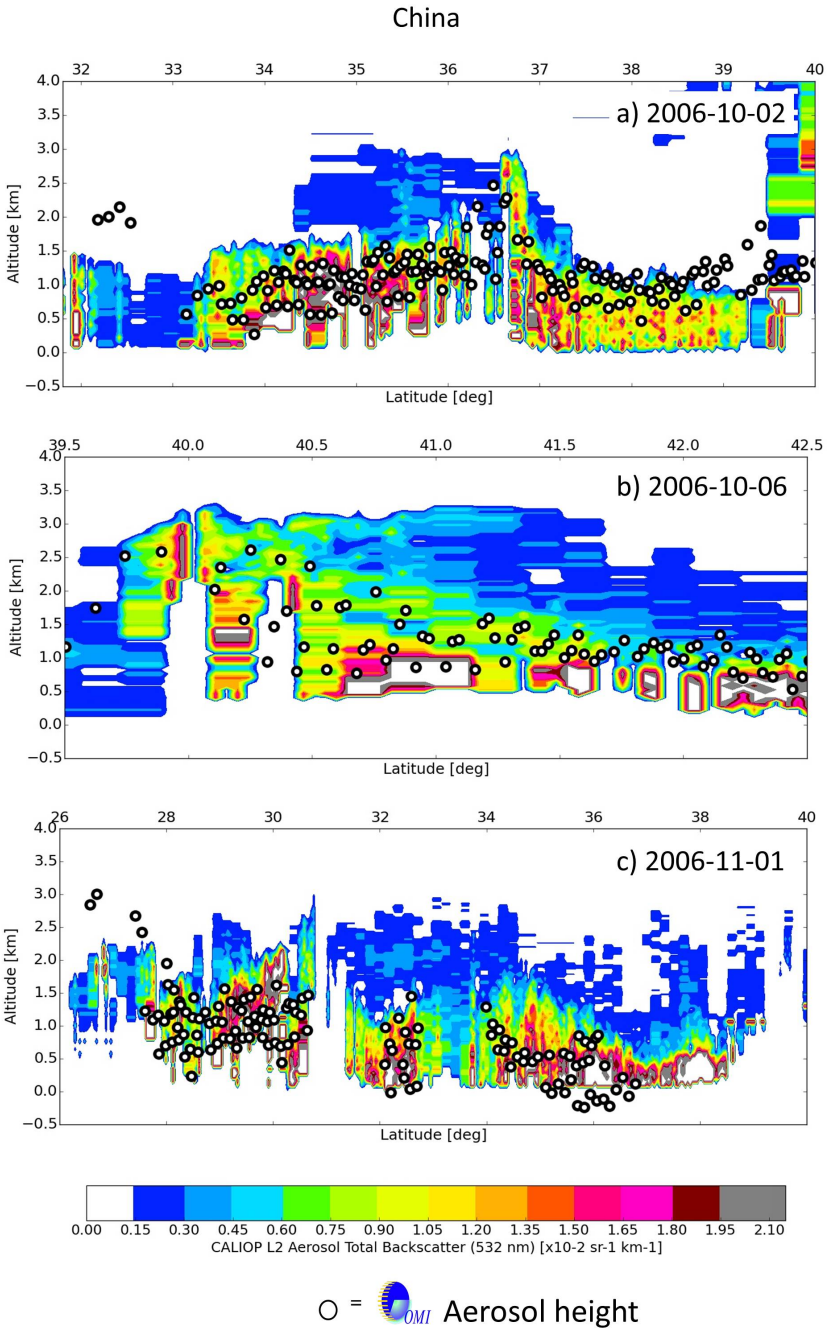

Figure 3. Retrieved OMI ALH compared with vertical profile of aerosol total backscatter coefficient (532 nm) from the CALIOP L2 product. Maximal distance between OMI pixels and CALIOP ground-track is 50 km. Only cloud-free OMI pixels, collocated with MODIS-Aqua Collection 6 aerosol cells, $\tau(550\text{nm}) \geq 0.55$ (from the MODIS DT DB algorithms), are selected: (**a**) 2006.10.02, (**b**) 2006.10.06, (**c**) 2006.11.01.

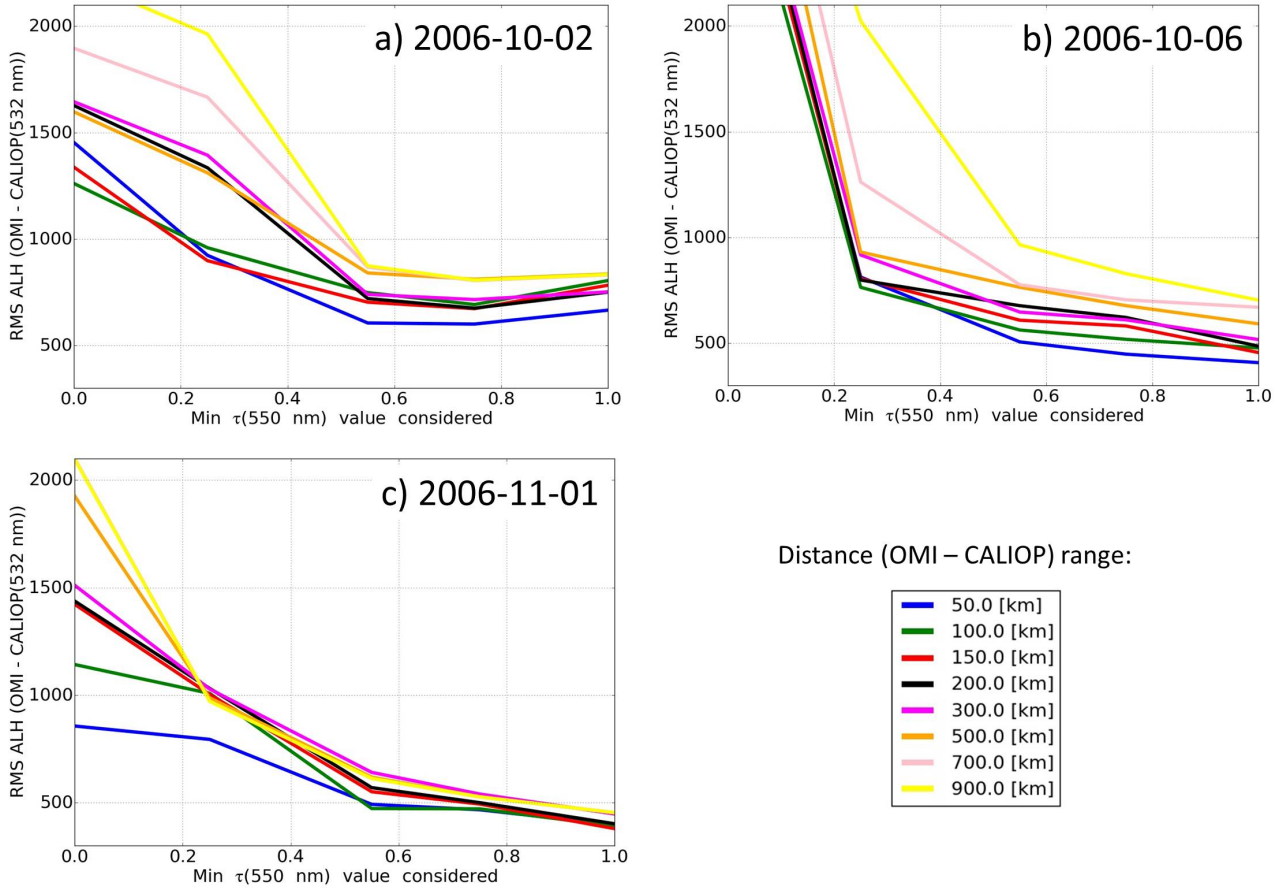

Figure 4. Root-mean-square (RMS) deviation between collocated retrieved OMI ALH and derived CALIOP ALH (532 nm) (see Sect. 4.1) for urban and industrialized cases over east China as a function of minimum MODIS $\tau(550\text{nm})$, and distance between OMI and CALIOP ground-pixels: (**a**) 2006.10.02, (**b**) 2006.10.06, (**c**) 2006.11.01.

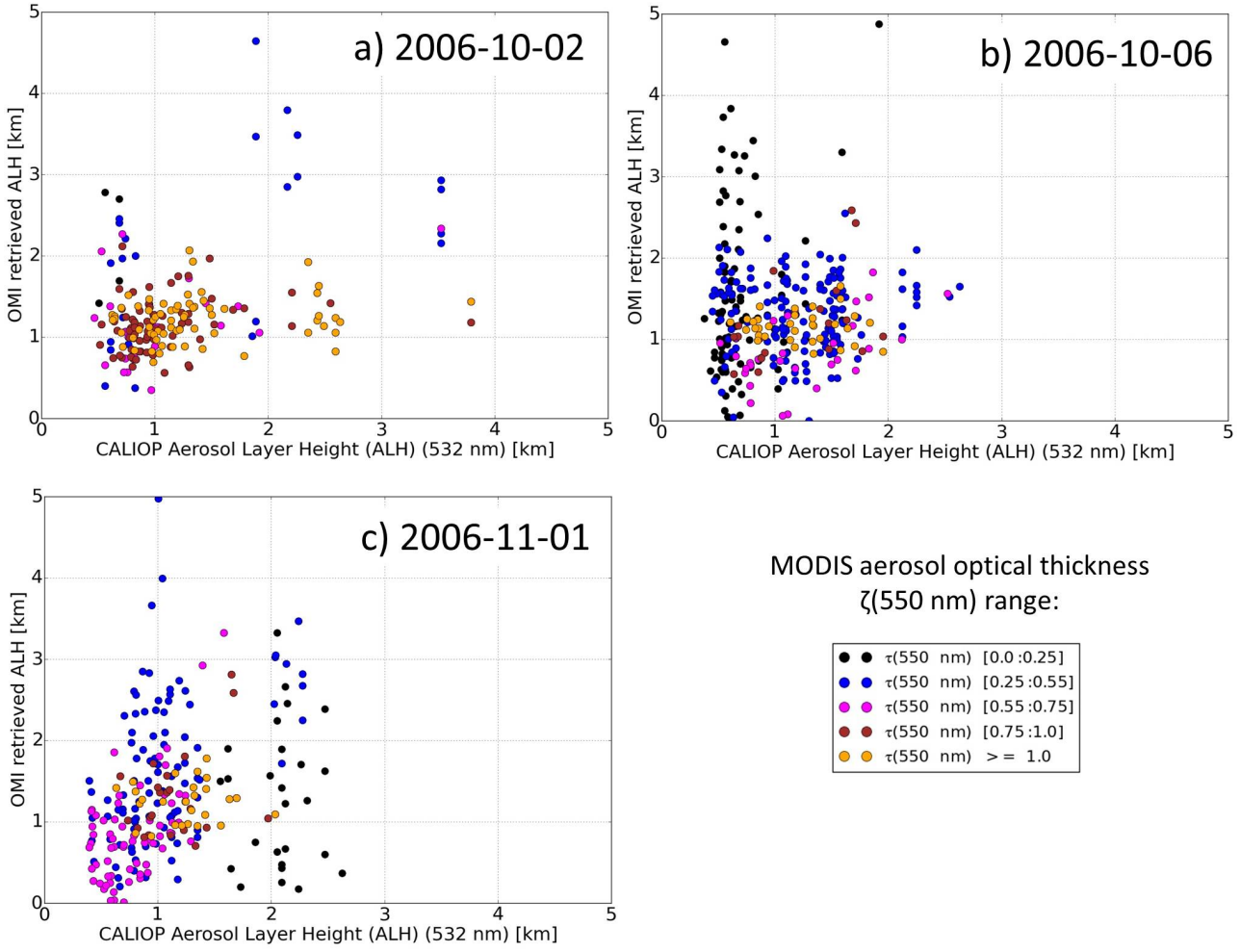

Figure 5. Scatter-plot of collocated retrieved OMI ALH and derived CALIOP ALH (532 nm) (see Sect. 4.1) for urban and industrialized cases over east China as a function of MODIS $\tau(550\text{nm})$. Distance between OMI and CALIOP pixels is 50 km: (**a**) 2006.10.02, (**b**) 2006.10.06, (**c**) 2006.11.01.

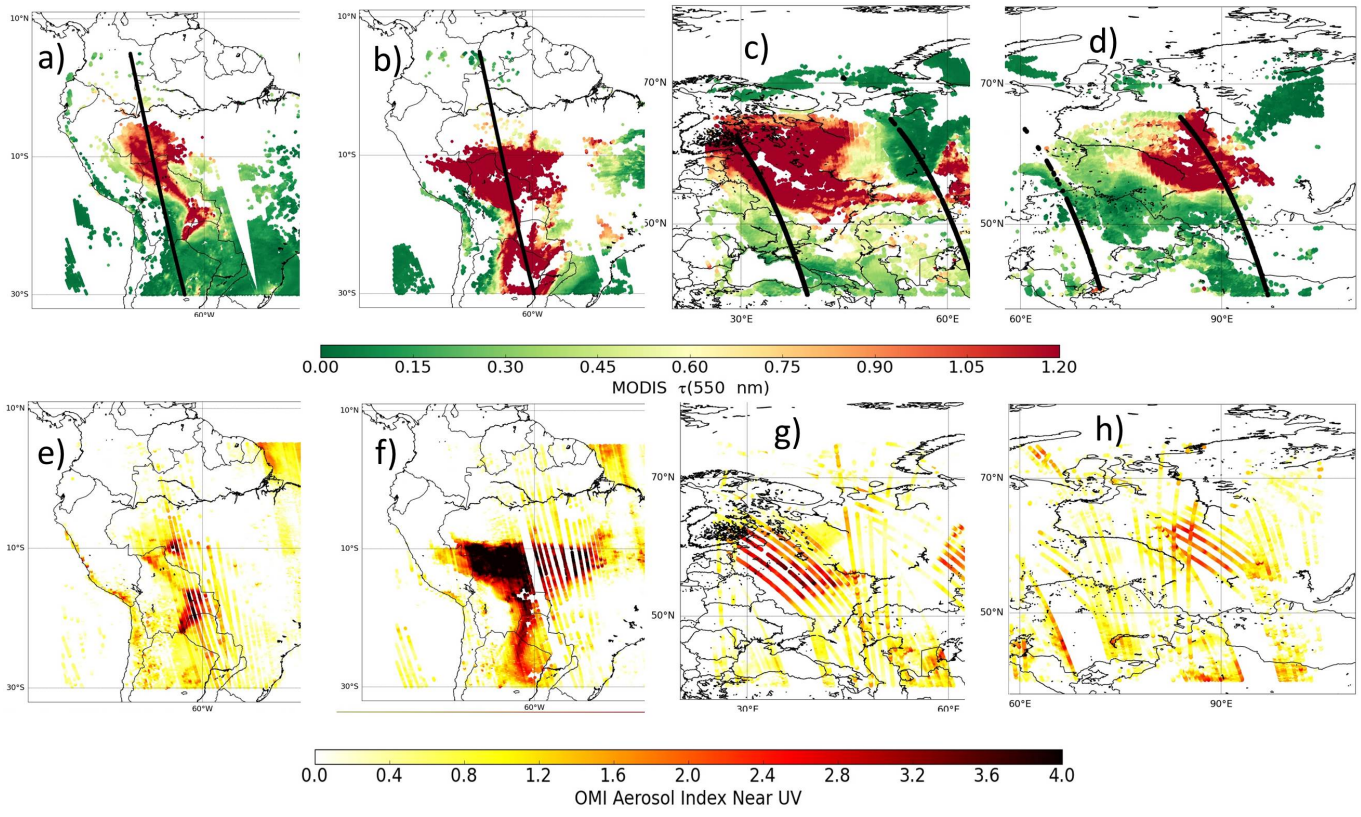

Figure 6. Maps of MODIS Aqua $\tau(550\text{nm})$ from the combined DT and DB Collection 6 (cf. Sect. 2.4), and collocated OMI aerosol index from near UV (UVAI) values (cf. Sect. 3) over cloud-free scenes and intensive biomass burning episodes. The dark thick lines represent the track of CALIPSO space-borne sensor over the selected case studies: (**a e**)South-America on 2006.08.24, (**b f**) South-America on 2007.09.30, (**c g**) east Russia on 2010.10.08, (**d h**) east Russia on 2012.06.23.

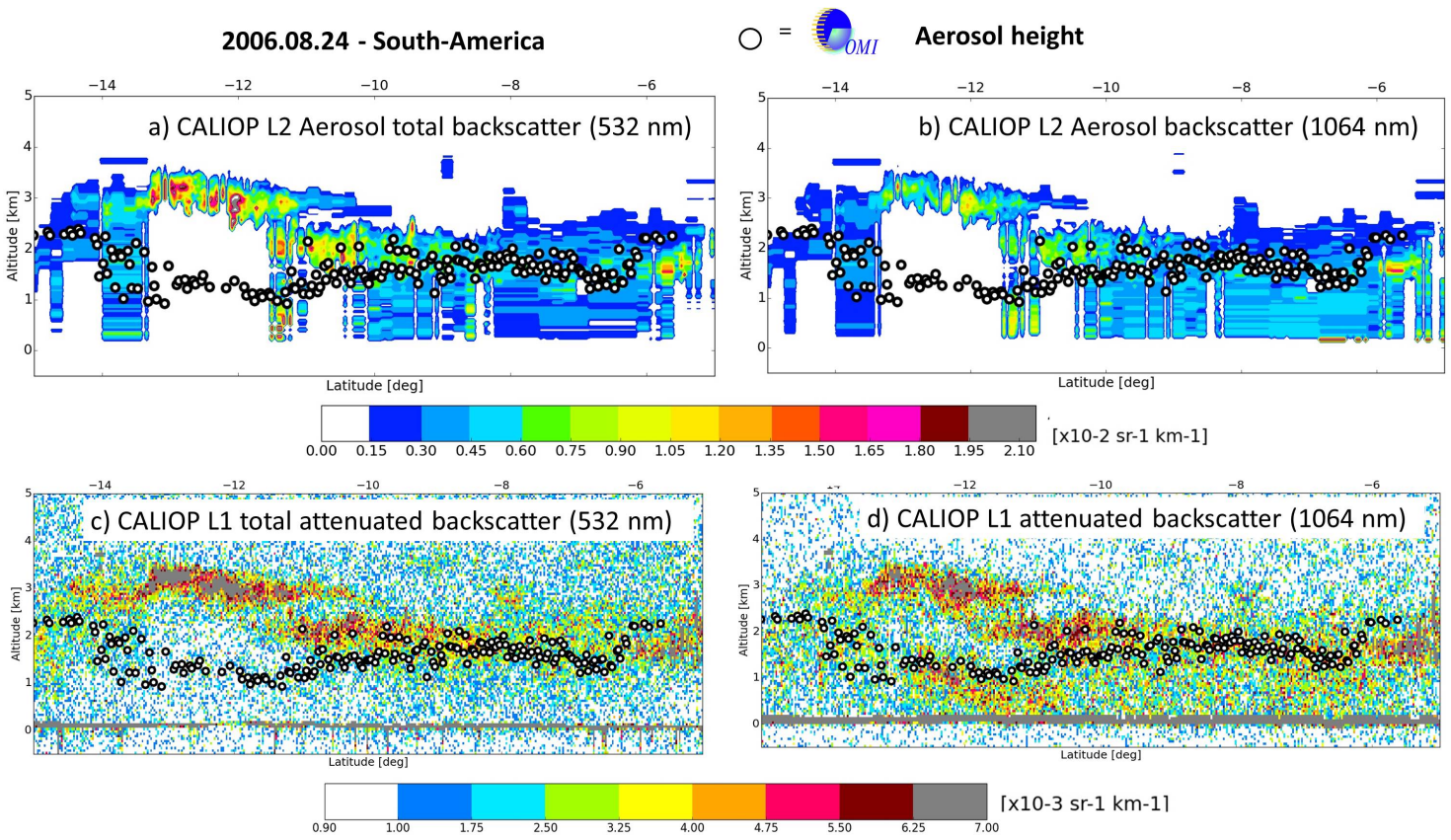

Figure 7. Retrieved OMI ALH compared with CALIOP along-track vertical profile observations for biomass burning case over South-America: (**a**) CALIOP L2 aerosol total backscattering (532 nm), (**b**) CALIOP L2 aerosol backscattering (1064 nm), (**c**) CALIOP L1 attenuated backscattering (532 nm), (**d**) CALIOP L1 attenuated backscattering (1064 nm).

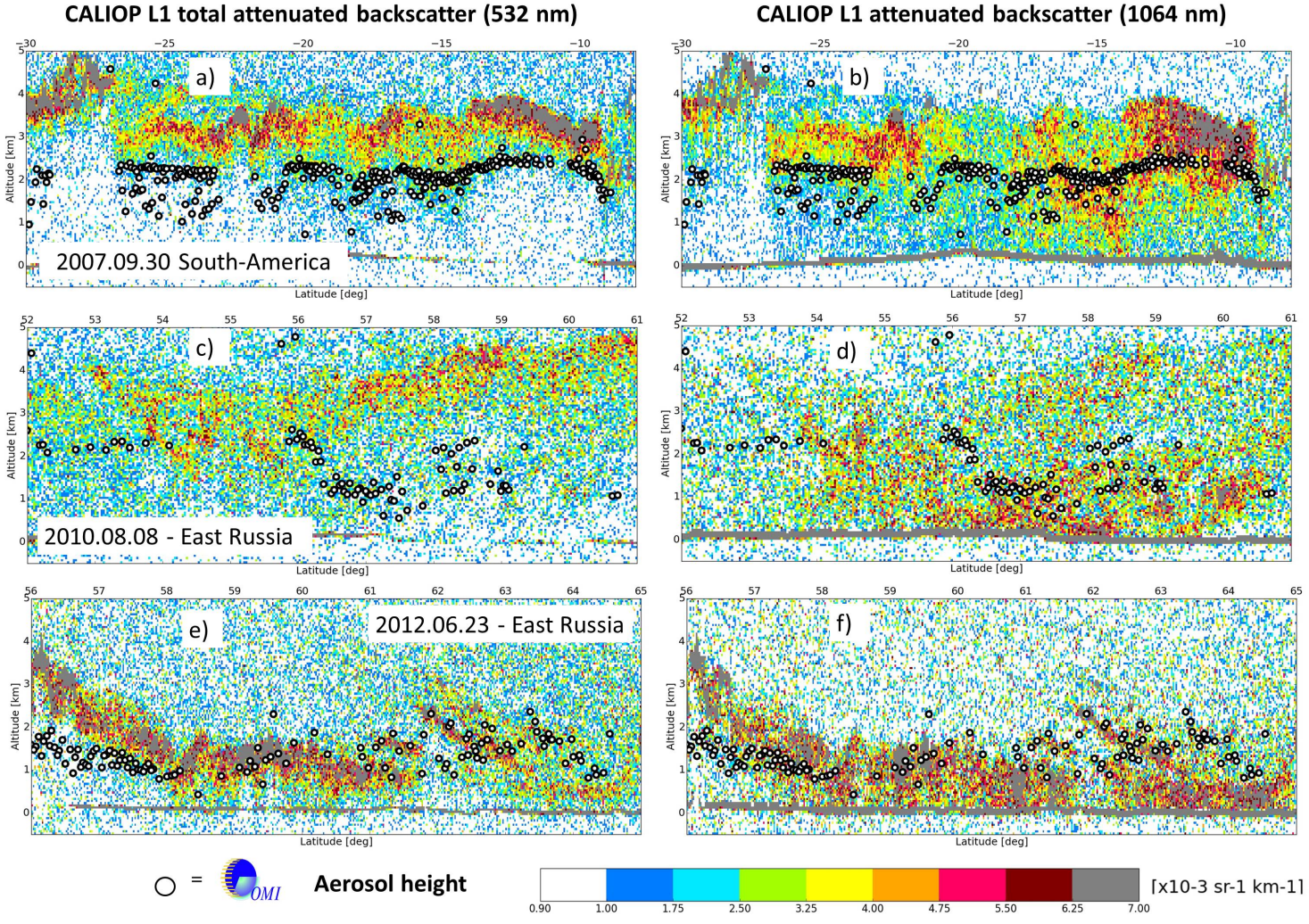

Figure 8. Retrieved OMI ALH compared with CALIOP L1 along-track vertical profile observations (532 and 1064 nm) for biomass burning cases: (**a b**) 2007.09.30 in South-America, (**c d**) 2010.08.08 in east Russia, (**e f**) 2012.06.23 in east Russia.

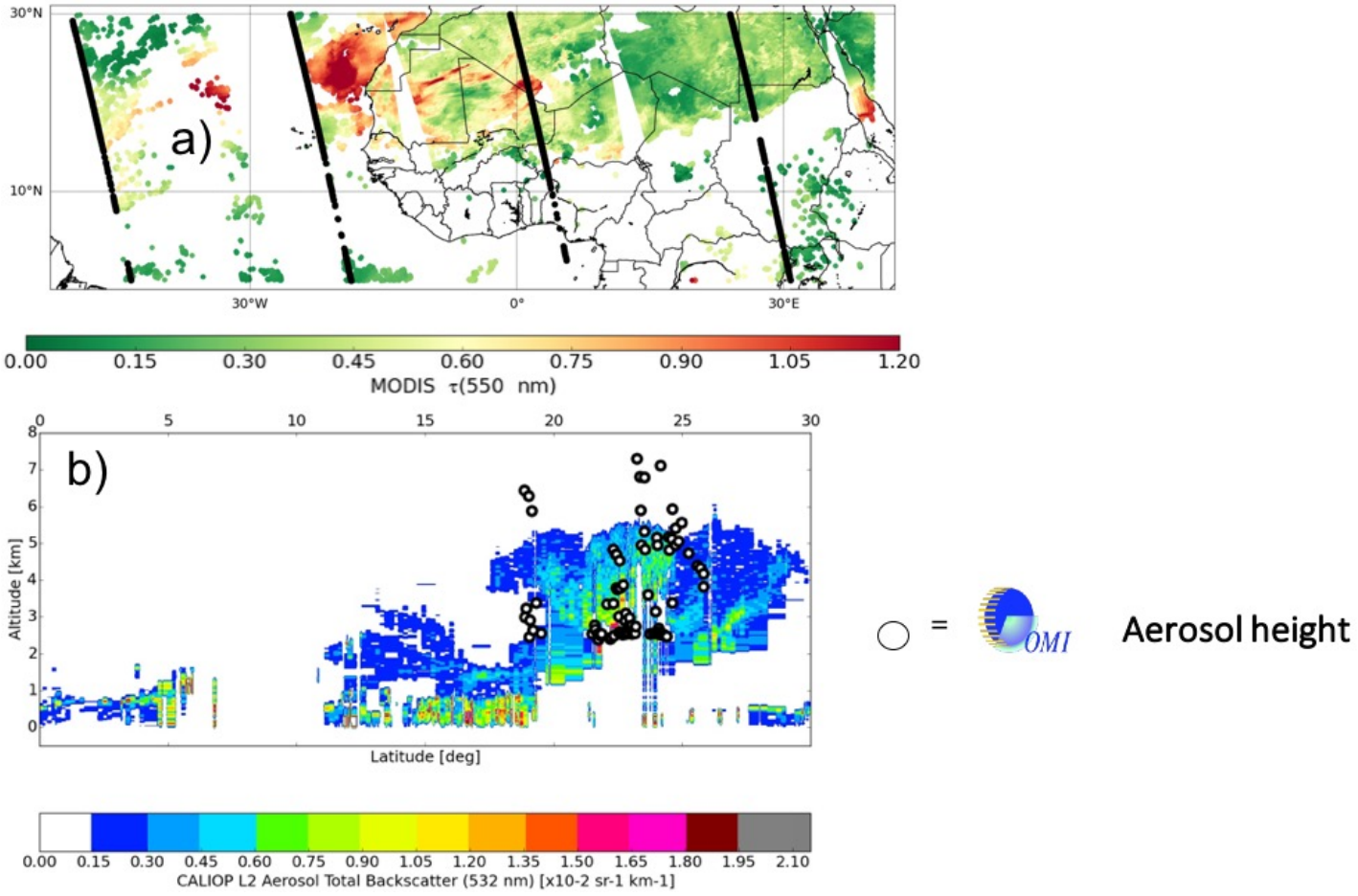

Figure 9. ~~Cloud-free case of an elevated~~ Elevated layer due to a Saharan dust outbreak transported to Western Meditterranean region over sea on ~~2012.06.28~~2007.07.19: (**a**) Map of MODIS Aqua $\tau(550\text{nm})$ from the combined DT DB Collection 6 (cf. Sect. 2.3), (**b**) Retrieved OMI ALH compared with vertical profile of aerosol total backscatter coefficient (532 nm) from the CALIOP L2 aerosol total backscatter (532 nm) associated with the ~~1st~~ 2nd left CALIPSO track over sea in Fig. 9a.

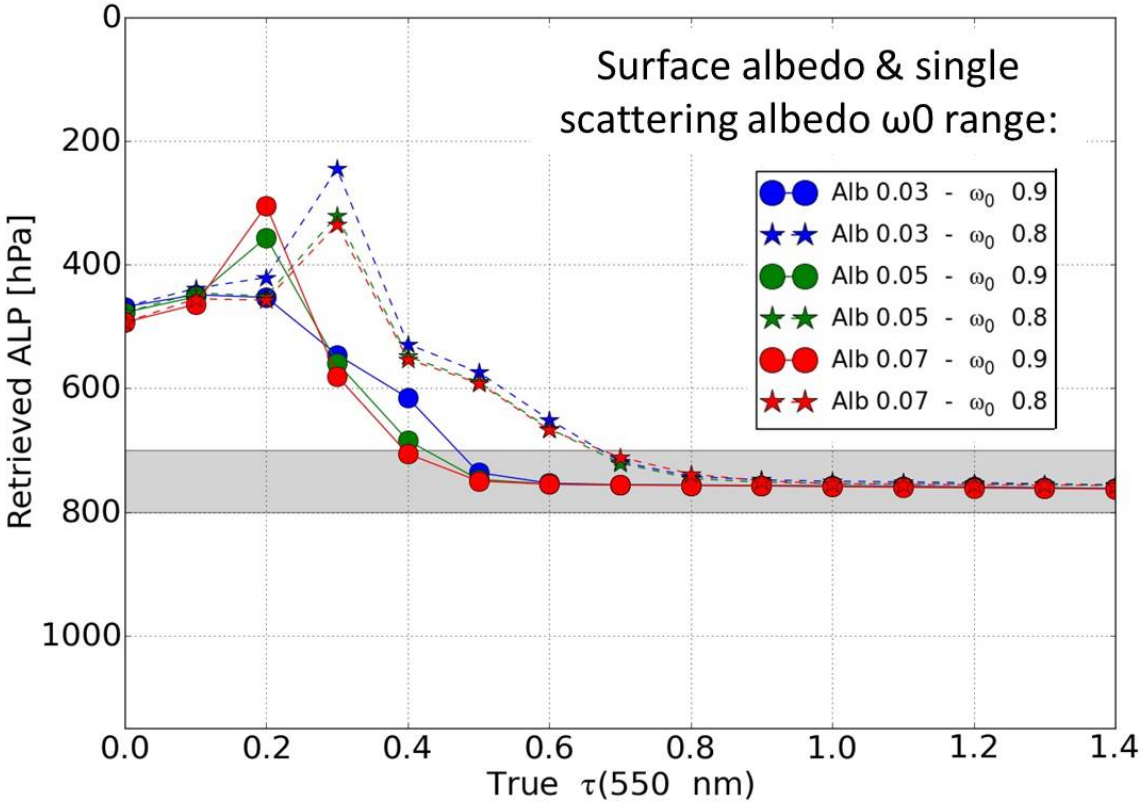

Figure 10. Simulated ALP retrievals, based on noise-free synthetic spectra with aerosols, as a function of true $\tau(550\mathrm{nm})$. All the retrievals are achieved with the NN algorithm trained with aerosol $\omega_0 = 0.9$ and true prior $\tau(550\mathrm{nm})$ value. The assumed geophysical conditions are temperature, H_2O, O_3 and NO_2 from climatology mid-latitude summer, $\theta_0 = 25°$, $\theta = 45°$ and $P_s = 1010\,\mathrm{hPa}$. The reference aerosol scenario assumes fine scattering particles ($\alpha = 1.5$, $g = 0.7$), and 2 aerosol ω_0 values: 0.9 and 0.8. Its location is depicted by the grey box, between 700 and 800 hPa.

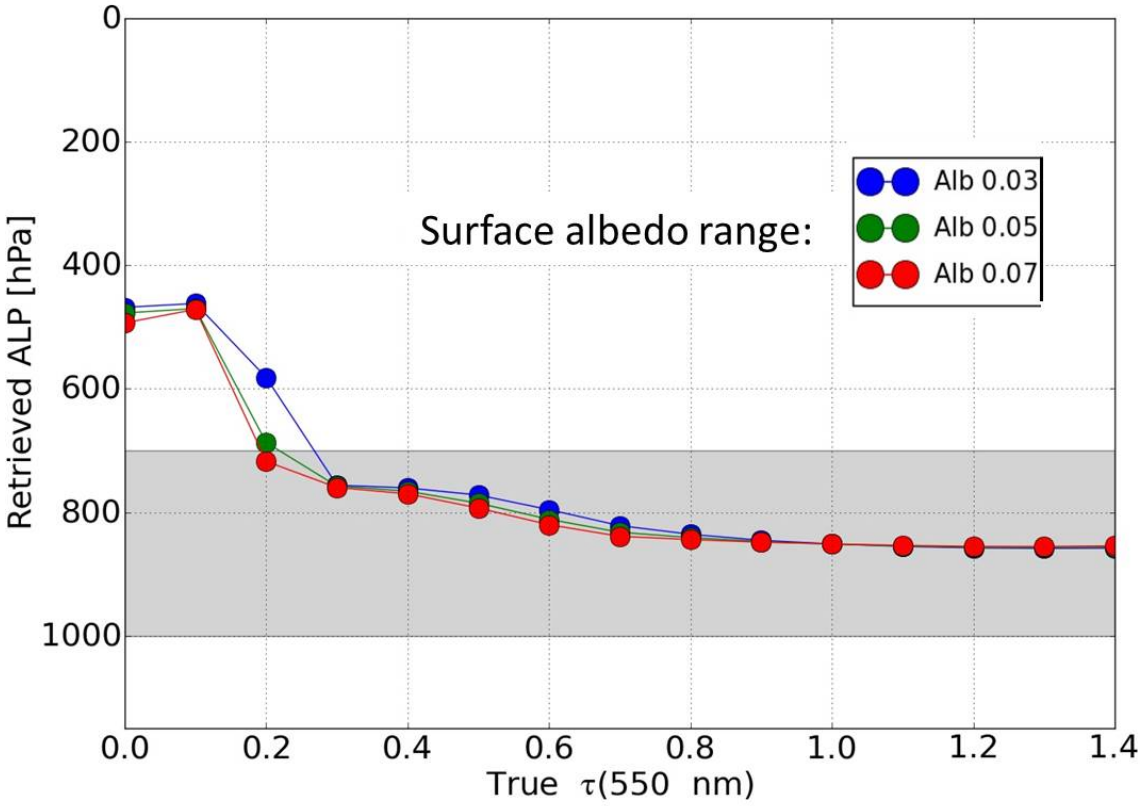

Figure 11. Same as Fig. 10 but with one unique aerosol ω_0 value (= 0.9) and a larger geometric extension of the aerosol layer included in the simulated spectra: i.e. between 700 and 1000 hPa.

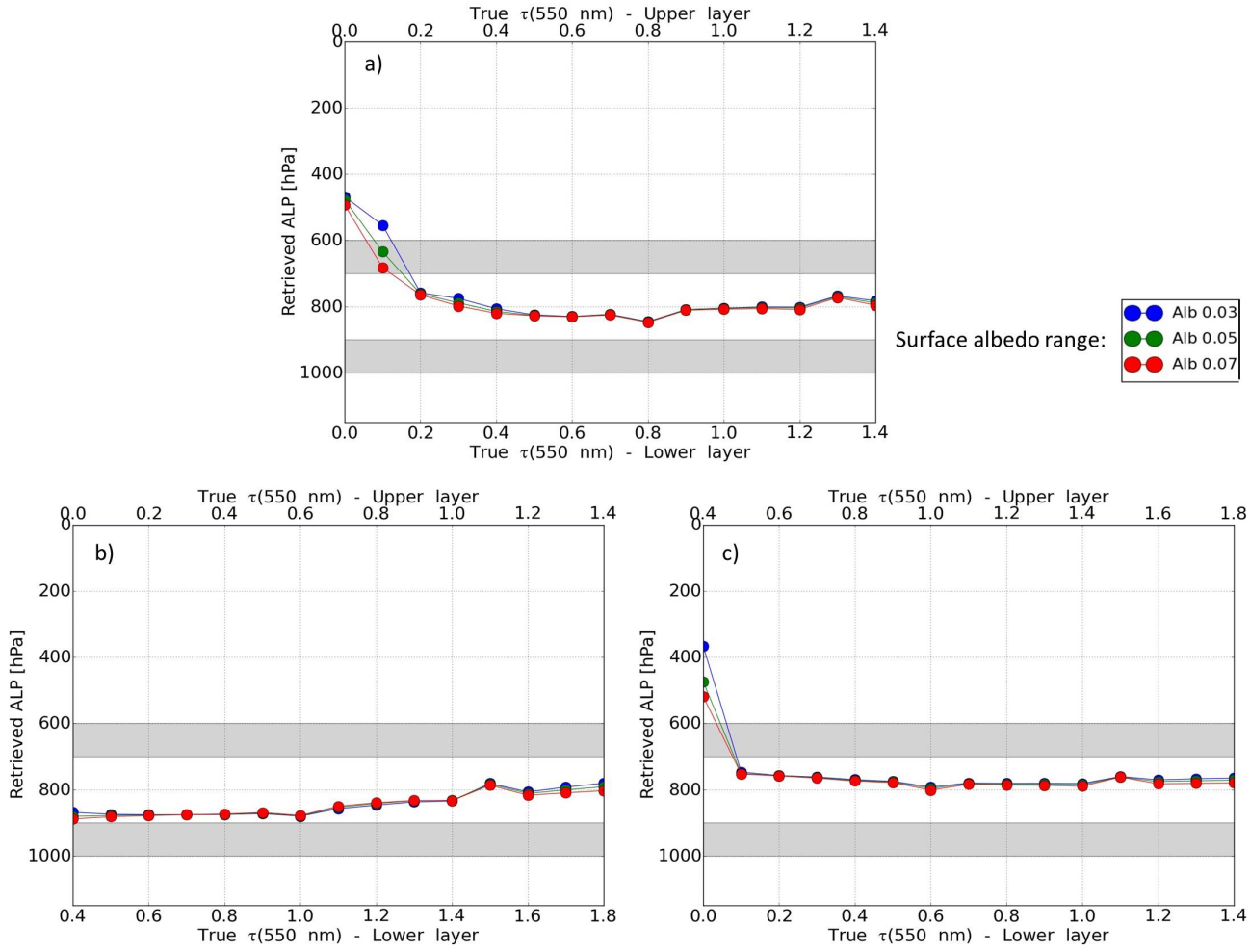

Figure 12. Same as Fig. 10 but with one unique aerosol ω_0 value (= 0.9) and 2 separate aerosol layers included in the simulated spectra. The bottom x-axis corresponds to the $\tau(550\mathrm{nm})$ value of the lower layer, while the top x-axis is the the $\tau(550\mathrm{nm})$ value of the upper layer. Both layers have same geometric thickness (i.e. 100 hPa). The first is located between 600 and 700 hPa, and the second is between 900 and 1000 hPa. **(a)** Both aerosol layers have same optical properties and $\tau(550\mathrm{nm})$ values, **(b)** Both aerosol layers have same optical properties but different $\tau(550\mathrm{nm})$ values: the lower layer has systematically a higher $\tau(550\mathrm{nm})$ (i.e. $+0.4$ for each scenario), **(b)** Both aerosol layers have same optical properties but different $\tau(550\mathrm{nm})$ values: the upper layer has systematically a higher $\tau(550\mathrm{nm})$ (i.e. $+0.4$ for each scenario)

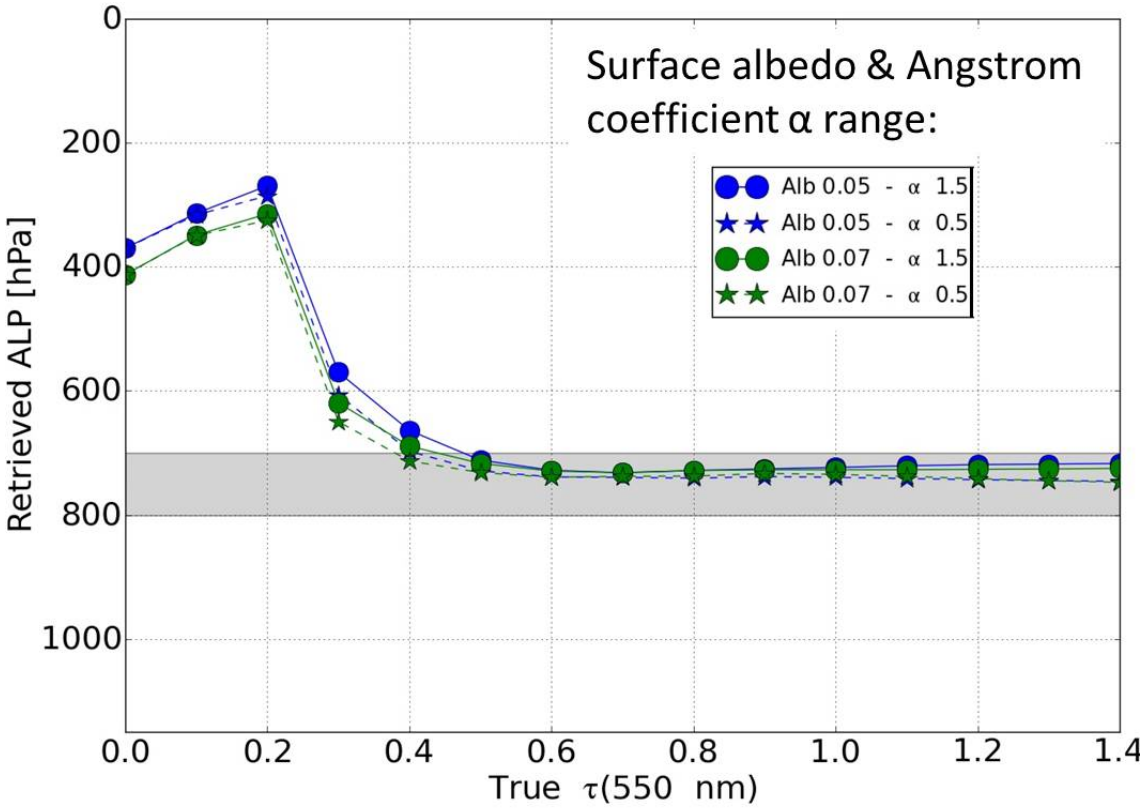

Figure 13. Same as Fig. 10 but with one unique aerosol ω_0 value (= 0.95) and two aerosol α (1.5 and 0.5) in the reference aerosol scenarios. ALP retrievals are estimated from the NN algorithm trained with aerosol ω_0 = 0.95 similarly to the desert dust case in Sect. 3.4.

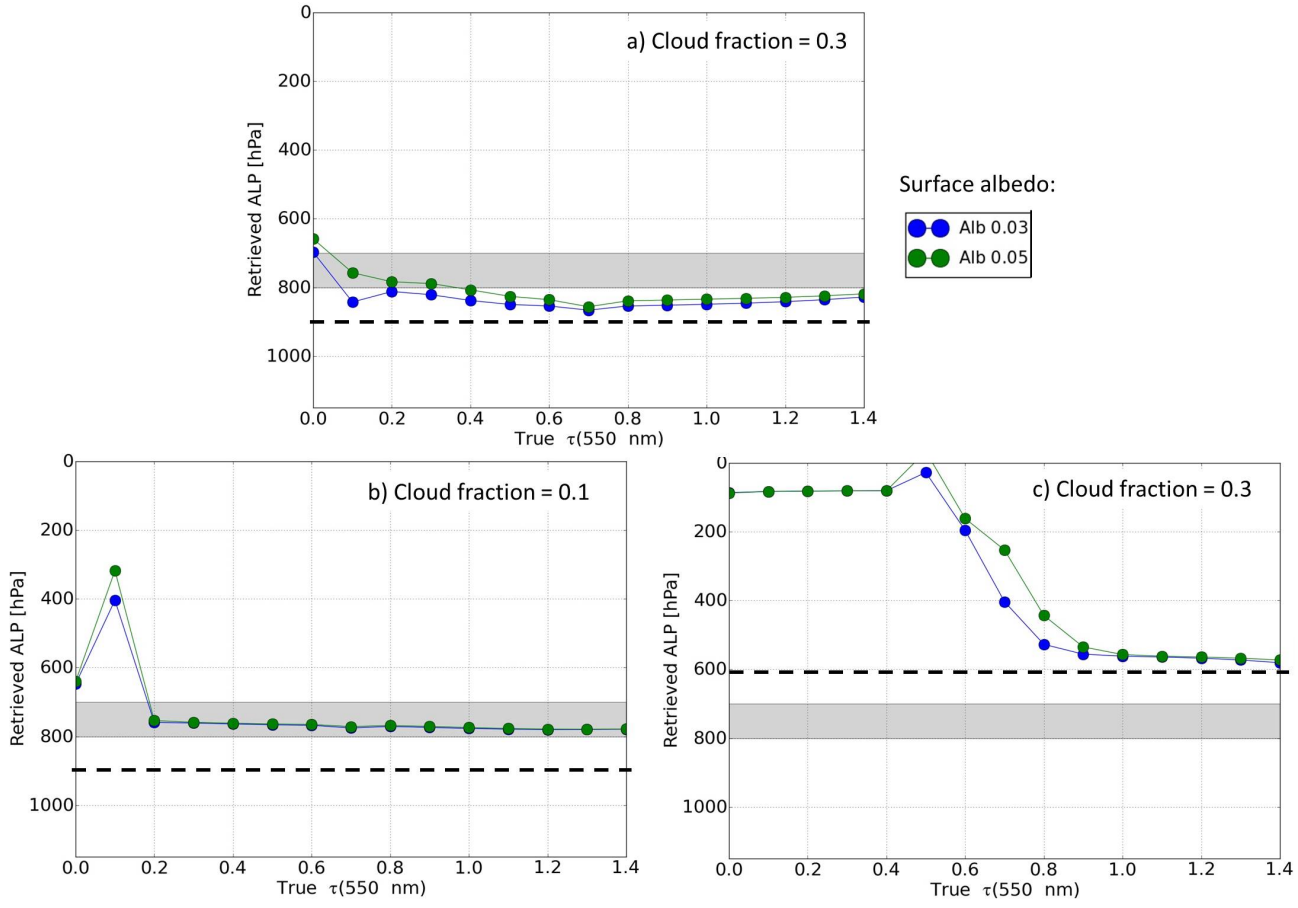

Figure 14. Same as Fig. 10 but with one unique aerosol ω_0 value (= 0.9) and the inclusion of a cloud (dashed thick black line) in addition to the aerosol layer. The cloud reflectance is simulated via a simple opaque (cloud albedo = 0.8) and Lambertian layer: **(a)** Effective cloud fraction = 0.3 and cloud pressure = 900 hPa, **(b)** Effective cloud fraction = 0.1 and cloud pressure = 900 hPa, **(a)** Effective cloud fraction = 0.3 and cloud pressure = 600 hPa.